Available online at www.sciencedirect.com

SCIENCE DIRECT®

Lithos 83 (2005) 317–346

LITHOS

www.elsevier.com/locate/lithos

Modeling of in-situ crystallization processes in the Permian mafic layered intrusion of Mont Collon (Dent Blanche nappe, western Alps)

Philippe Monjoie[a,b], François Bussy[a,*], Henriette Lapierre[b], Hans-Rudolf Pfeifer[a]

[a]*Institute of Mineralogy and Geochemistry, BFSH2, University of Lausanne, CH-1015 Lausanne, Switzerland*
[b]*Laboratoire Géodynamique des Chaînes Alpines, UMR-CNRS 5025, Université Joseph Fourier, Géosciences, B.P. 53, 38041 Grenoble Cedex, France*

Received 29 December 2003; accepted 18 February 2005
Available online 27 April 2005

Abstract

The Mont Collon mafic complex is one of the best preserved examples of the Early Permian magmatism in the Central Alps, related to the intra-continental collapse of the Variscan belt. It mostly consists (>95 vol.%) of ol+hy-normative plagioclase-wehrlites, olivine- and cpx-gabbros with cumulitic structures, crosscut by acid dikes. Pegmatitic gabbros, troctolites and anorthosites outcrop locally. A well-preserved cumulative sequence is exposed in the Dents de Bertol area (center of intrusion). *P–T* calculations indicate that this layered magma chamber emplaced at mid-crustal levels at about 0.5 GPa and 1100 °C. The Mont Collon cumulitic rocks record little magmatic differentiation, as illustrated by the restricted range of clinopyroxene mg-number ($Mg\#_{cpx}$=83–89). Whole-rock incompatible trace-element contents (e.g. Nb, Zr, Ba) vary largely and without correlation with major-element composition. These features are characteristic of an in-situ crystallization process with variable amounts of interstitial liquid *L* trapped between the cumulus mineral phases. LA-ICPMS measurements show that trace-element distribution in the latter is homogeneous, pointing to subsolidus re-equilibration between crystals and interstitial melts. A quantitative modeling based on Langmuir's in-situ crystallization equation successfully duplicated the REE concentrations in cumulitic minerals of all rock facies of the intrusion. The calculated amounts of interstitial liquid *L* vary between 0 and 35% for degrees of differentiation *F* of 0 to 20%, relative to the least evolved facies of the intrusion. *L* values are well correlated with the modal proportions of interstitial amphibole and whole-rock incompatible trace-element concentrations (e.g. Zr, Nb) of the tested samples. However, the in-situ crystallization model reaches its limitations with rock containing high modal content of REE-bearing minerals (i.e. zircon), such as pegmatitic gabbros. Dikes of anorthositic composition, locally crosscutting the layered lithologies, evidence that the Mont Collon rocks evolved in open system with mixing of intercumulus liquids of different origins and possibly contrasting compositions. The proposed model is not able to resolve these complex open systems, but migrating liquids could be partly responsible for the observed dispersion of points in some

* Corresponding author. Tel.: +41 21 6924458; fax: +41 21 6924305.
E-mail address: francois.bussy@unil.ch (F. Bussy).

doi:10.1016/j.lithos.2005.03.008

correlation diagrams. Absence of significant differentiation with recurrent lithologies in the cumulitic pile of Dents de Bertol points to an efficiently convective magma chamber, with possible periodic replenishment.

Keywords: Layered gabbro; In-situ crystallization; Permian; Basic magmatism; LA-ICPMS; Interstitial melt

1. Introduction

Three distinct magmatic events characterized the end of the Variscan orogeny: Early Carboniferous, Late Carboniferous–Early Permian, and Late Permian. In the Early Carboniferous, acidic intrusions were emplaced in strike-slip faults zones in the basement areas of the Alpine realm, such as the External Crystalline Massifs (Bonin et al., 1993; Debon et al., 1994; von Raumer et al., 1993; Bussy et al., 2000). At the Carboniferous–Permian boundary, the end of the Variscan Range collapse is marked by the emplacement of several mantle-derived mafic complexes and K-rich magmas related to intra-continental extension and crustal thinning (e.g. Dal Piaz, 1993). In the Western and Central Alpine belt, this mafic magmatism is essentially distributed in the Austroalpine and South Alpine domains, represented by the so-called Permian Mafic Complexes (=PMC) of Val Malenco (281 ± 19 Ma, Hansmann et al., 2001; Hermann and Rubatto, 2003), Sondalo (300 ± 12 and 280 ± 10 Ma, Tribuzio et al., 1999), Ivrea–Verbano (285–290 Ma, Rivalenti et al., 1980; Sinigoi et al., 1994; Mulch et al., 2002) and Mont Collon (284 ± 0.6 Ma, Monjoie et al., submitted for publication). Large parts of the Variscan belt have been involved in the Alpine orogeny and some of them underwent high-grade metamorphic recrystallization and deformation. In contrast, the Mont Collon gabbroic intrusion, which belongs to the lower tectonic unit of the Dent Blanche nappe system, displays remarkably well-preserved magmatic structures and mineral assemblages, which allow detailed investigation and modeling of crystallization processes in an intra-continental mafic magma chamber. Our new petrological and chemical data indicate a transitional MORB-type affinity for the Mont Collon intrusion. Monotonous major-element compositions throughout the intrusion coupled to highly variable trace-element distribution are best explained by an in-situ crystallization model, in which the relative proportion of interstitial residual liquid can be computed.

2. Geological background and field relationships

The European Alpine belt is classically subdivided into four main tectonic domains, i.e. from west to east: the Helvetic–UltraHelvetic, Penninic, Austroalpine and southern Alpine domains, respectively (Fig. 1). In the western Alps, the Austroalpine domain or system is subdivided into two main geographically disconnected units: the Sesia–Lanzo zone (internal SE part) and the Dent-Blanche nappe s.l. (external NW part) (Martinotti and Hunziker, 1984; Venturini et al., 1996; Dal Piaz, 1999), which consists of several independent klippes overlapping all other Alpine nappes. The largest klippe, known as the Dent-Blanche Nappe s.s., comprises two pre-Mesozoic basement units: the tectonically upper Valpelline and lower Arolla Series, respectively. The Arolla Series is the country rock of the Mont Collon mafic complex. It is made of high-grade paragneisses and fine-grained metabasites intruded by late Paleozoic granitoids (now orthogneisses, ca. 289 Ma; Bussy et al., 1998) affected by greenschist facies Alpine re-equilibration.

The Mont Collon mafic complex is exposed over ca. 14 km^2 within the Arolla Series of the Dent Blanche nappe s.s., near the village of Arolla, Wallis, Switzerland. Outcrops are discontinuous in-between large glaciers and moraines (Fig. 2), which makes lateral and vertical correlations difficult to establish. Contact with the country rock is mylonitic and refolded with both the orthogneisses and the gabbroic rocks deformed by Alpine tectonics. It is not quite clear whether the Arolla orthogneisses represent the original country rock of the intrusion or not. The Alpine greenschist facies metamorphic overprint in the intrusion is weak, but increases towards the mylonitic contact.

A well-preserved sub-vertical magmatic layering is exposed over several hundred meters in the center of the intrusion (Dents de Bertol). It is defined by a monotonous rhythmic alternation of olivine- and clinopyroxene-bearing gabbro layers of variable thickness. Other rock types include two 2-m-thick isolated

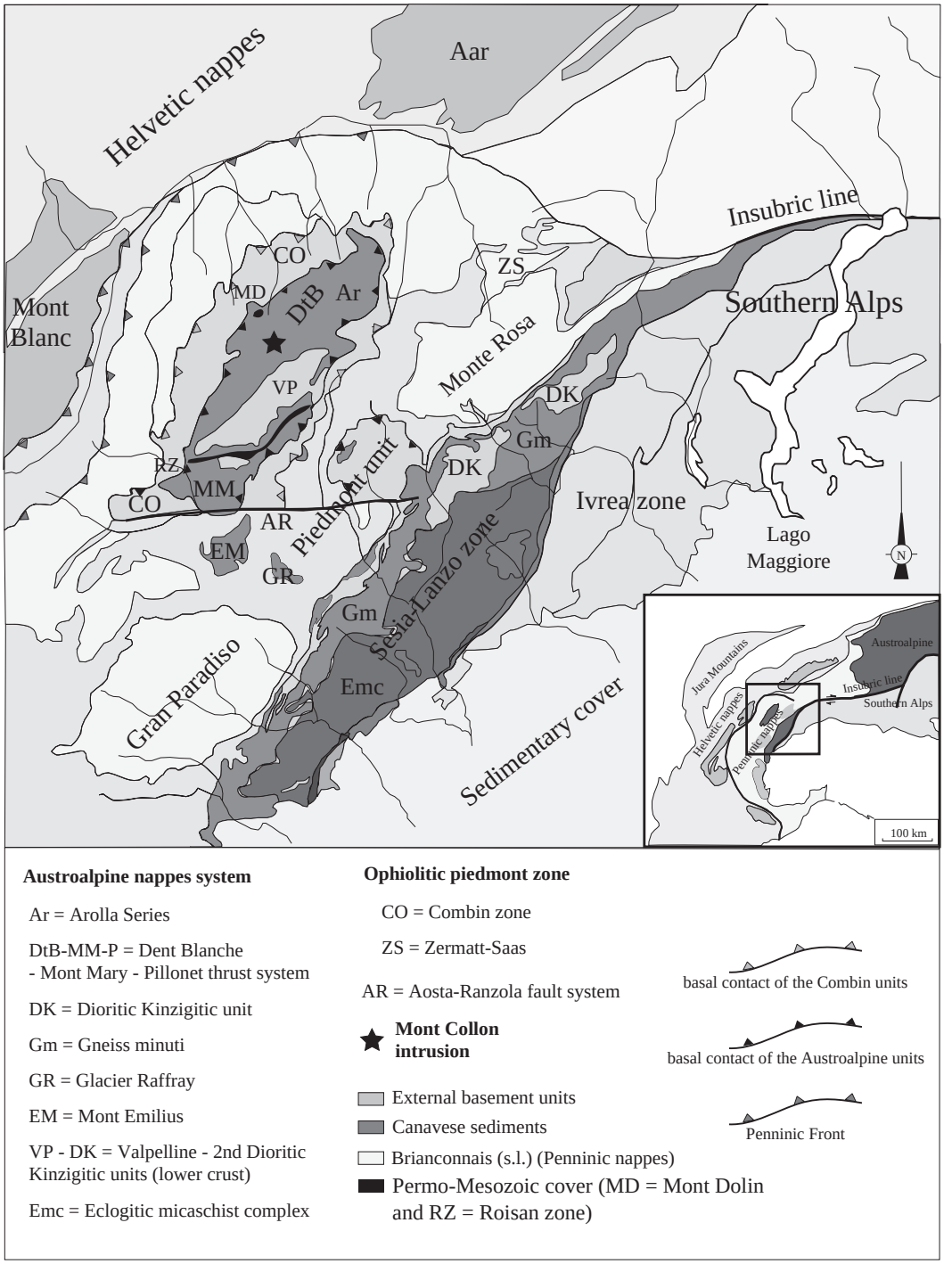

Fig. 1. Tectonic map of the northwestern Alps (after Bigi et al., 1990; Dal Piaz, 1993, 1999) showing the main tectonic units, i.e.: the Helvetic nappes, the External Crystalline Massifs (Mont Blanc, Aiguilles Rouges and Aar-Gotthard massifs), the klippe of the Dent Blanche nappe, the Piedmont units, the Internal Crystalline massifs of the Gran Paradiso and the Monte Rosa, the Sesia–Lanzo zone and the southern Alpine unit of Ivrea. Inset: Main tectonic units of the northwestern Alps.

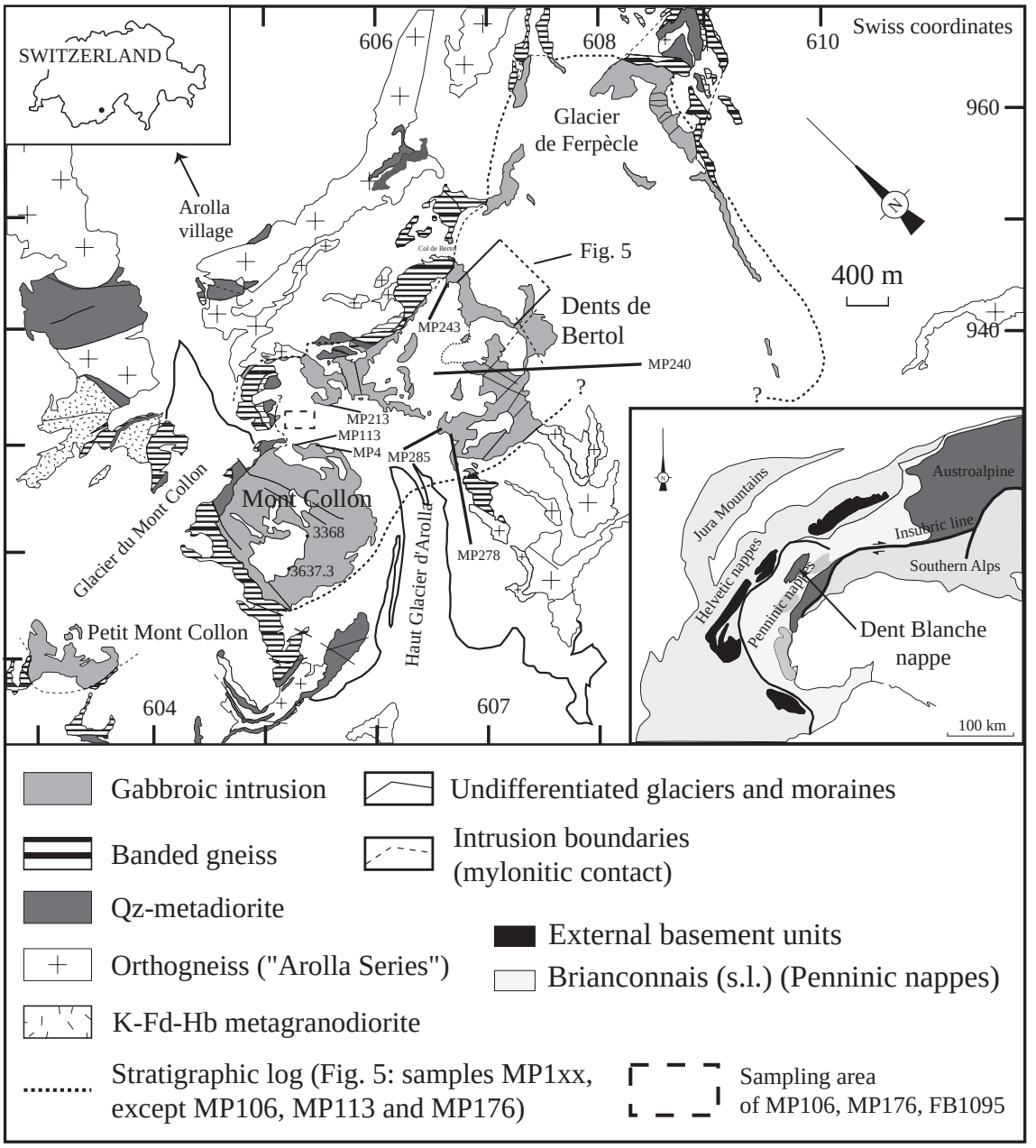

Fig. 2. Geological map of the Mont Collon area (scale 1:25 000), modified after the "Matterhorn" geological map no. 1347, from the Geological Atlas of Switzerland (Bucher et al., 2003, 2004). Inset: Main tectonic units of the northwestern Alps.

melanocratic layers of wehrlite and a single layer of anorthosite. Other facies of interest outside the layered sequence consist of sills of wehrlite parallel to the gabbro layering, as well as a few meter-sized pockets of pegmatitic gabbros, which represent the only mafic facies without cumulitic features. They are disconnected from the other lithologies and are randomly distributed in the massif.

Dykes are widespread in the Mont Collon intrusion and systematically crosscut the gabbroic facies (Dal Piaz et al., 1977). Most are leucocratic, cm- to dm-thick and of monzonitic, granitic or anorthositic composition. A few are black, meter-thick alkaline lamprophyres of younger age (260 Ma by $^{39}Ar/^{40}Ar$ dating on pargasite, Monjoie et al., submitted for publication). Granitic dykes are thought to be melts derived from the partial fusion of the country rock (i.e. the Arolla orthogneisses) in relation with the intrusion of the gabbros (back-veining).

3. Petrography

Most rocks of the Mont Collon intrusion are well-preserved medium- to coarse-grained cumulates (Fig. 3), displaying variable modal amounts of olivine,

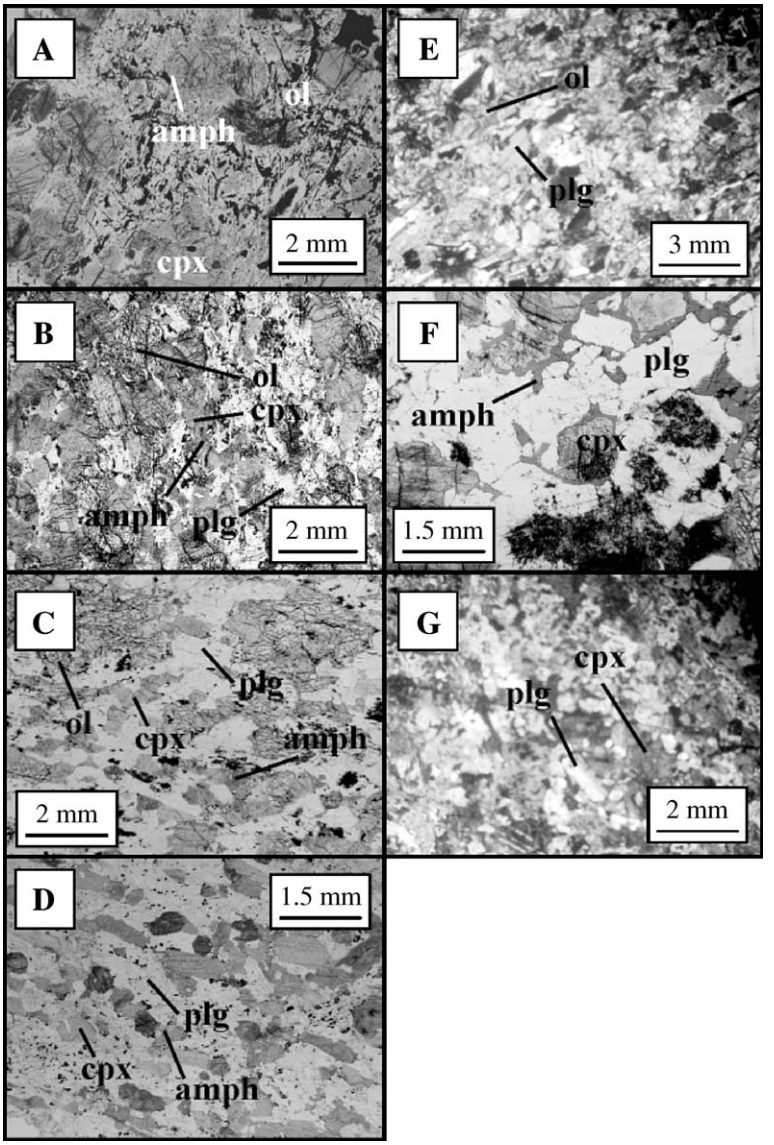

Fig. 3. Microphotographs of thin sections of the Mont Collon cumulates (LN). (A) Wehrlite, (B) plg-wehrlite, (C) ol-gabbro, (D) cpx-gabbro, (E) troctolite, (F) example of interstitial magmatic amphibole in ol-gabbro and (G) anorthosite.

clinopyroxene and plagioclase as major mineral constituents (see major-element composition of minerals in Tables 1–5 and profiles along mean mineral compositions in Fig. 4). Plagioclase-wehrlites, olivine- and clinopyroxene-bearing gabbros are the most common facies (about 95 vol.%) with some rare wehrlites and troctolites. They crop out as variable sized layers forming a well-defined cumulate sequence in the Dents de Bertol area. Well-preserved cumulitic textures are underlined by preferred mineral orientation. Olivine and clinopyroxene form the main cumulus phases and crystallize as 2–3 mm long eu- to subhedral grains. Plagioclase forms tabular crystals, commonly with parallel alignment. Late-magmatic Ti-amphibole dominates the intercumulus assemblage, occurring as overgrowths or patches surrounding clinopyroxene. Accessory minerals (magnetite, ilmenite, sulphides and apatite) are rare in all lithologies.

Wehrlites are mesocumulates with highly serpentinized olivine (up to 60 vol.%) and euhedral diopsidic clinopyroxene as cumulus phases and intercumulus magnesio-hastingsitic hornblende, which almost completely recrystallized into actinolite–tremolite.

Olivine is the main cumulus phase **in plagioclase-bearing wehrlites** and displays a constant composition (Fo 75.3 to 77.8) with Ni content between 450 and 630 ppm. MnO shows constant concentration close to 0.3 wt.%. Euhedral to subhedral clinopyroxene represents 20–30% of the cumulus phases. Its composition varies from endiopside in the core to diopside in the rim, i.e. $Mg\#_{cpx}$ decreases from 83 to 87 and CaO increases from 22.0% to 23.2%, respectively. Clinopyroxene has a higher Al_2O_3 content in plagioclase-bearing wehrlites than in gabbros. It varies from 2.9% to 3.9% and generally decreases from core to rim, while Na_2O and TiO_2 increase. Variable modal proportions (10–30%) of labradoritic plagioclase ($An_{63.1}$ and $An_{69.2}$) appear as an intercumulus phase. A significant amount of a magnesio-hastingsite magmatic amphibole fills the interstices between plagioclase and clinopyroxene or occurs locally as large patches surrounding the latter minerals.

Table 1
Representative major-element compositions of olivines from plg-wehrlites, troctolite and ol-gabbros

Rock types	Plg-wehrlite				Troctolite				Ol-gabbros					
Sample numbers	MP106		FB1095		MP240				MP125		MP136		MP161	
	Core	Rim	Core	Rim	Core	Rim	Core	Rim	Core	Rim	Core	Rim	Core	Rim
SiO_2	38.1	38.3	39.4	39.4	39.2	39.1	38.9	39.1	38.8	38.8	38.7	38.3	38.5	38.8
TiO_2	0.01	0.01	0.01	0.01	0.02	0.00	0.01	0.01	0.03	0.02	0.03	0.01	0.01	0.00
Al_2O_3	0.01	0.01	0.01	0.00	0.01	0.01	0.02	0.02	0.00	0.00	0.00	0.01	0.00	0.01
Cr_2O_3	0.01	0.02	0.00	0.02	0.02	0.01	0.02	0.02	0.06	0.01	0.04	0.00	0.01	0.02
FeO_T	22.6	22.2	20.7	20.6	19.3	19.8	19.9	19.8	19.3	19.6	20.6	21.1	21.9	21.9
MnO	0.35	0.41	0.32	0.32	0.26	0.26	0.29	0.28	0.31	0.30	0.30	0.31	0.34	0.34
MgO	38.6	39.2	40.6	40.4	41.6	41.9	41.3	41.4	41.7	41.7	41.3	41.1	39.7	39.9
CaO	0.04	0.03	0.07	0.06	0.03	0.00	0.01	0.03	0.00	0.01	0.02	0.07	0.04	0.05
NiO	0.07	0.05	0.05	0.06	0.06	0.05	0.06	0.07	0.04	0.02	0.08	0.07	0.04	0.07
Total	99.8	100.3	101.0	100.9	100.4	101.1	100.5	100.6	100.2	100.4	101.0	101.1	100.5	101.1
Si	0.996	0.995	1.004	1.005	1.000	0.994	0.995	0.997	0.994	0.993	0.989	0.982	0.994	0.996
Ti	0.000	0.000	0.000	0.000	0.000	0.000	0.000	0.000	0.001	0.000	0.000	0.000	0.000	0.000
Al^{IV}	0.000	0.000	0.000	0.000	0.000	0.000	0.001	0.001	0.000	0.000	0.000	0.000	0.000	0.000
Al^{VI}	0.000	0.000	0.000	0.000	0.000	0.000	0.000	0.000	0.000	0.000	0.000	0.000	0.000	0.000
Cr	0.000	0.000	0.000	0.000	0.000	0.000	0.000	0.000	0.001	0.000	0.001	0.000	0.000	0.000
Fe^{2+}	0.493	0.482	0.440	0.440	0.411	0.421	0.426	0.424	0.412	0.418	0.440	0.453	0.473	0.470
Mn	0.008	0.009	0.007	0.007	0.006	0.006	0.006	0.006	0.007	0.007	0.006	0.007	0.007	0.007
Mg	1.504	1.517	1.541	1.538	1.582	1.585	1.576	1.574	1.590	1.587	1.572	1.571	1.529	1.527
Ca	0.001	0.001	0.002	0.002	0.001	0.000	0.000	0.001	0.000	0.000	0.000	0.002	0.001	0.001
Ni	0.001	0.001	0.001	0.001	0.001	0.001	0.001	0.001	0.001	0.000	0.002	0.001	0.001	0.001
Fa	24.7	24.1	22.2	22.2	20.6	21.0	21.3	21.2	20.6	20.8	21.9	22.4	23.6	23.5
Fo	75.3	75.9	77.8	77.8	79.4	79.0	78.7	78.8	79.4	79.2	78.1	77.6	76.4	76.5

Structural formula based on 3 cations. Measurements were made on a Cameca SX50 electron microprobe at 15 kV and a beam current of 30 nA. Olivines from wehrlites are all serpentinized and not included in this table.

Table 2
Representative major-element compositions of clinopyroxenes from wehrlites, plg-wehrlites, troctolite, ol- and cpx-gabbros and anorthosite

Rock types	Wehrlite		Plg-wehrlite						Troctolite				Ol-gabbros								Cpx-gabbros						Anorthosite	
Sample numbers	MP243		MP106		FB1094		FB1095		MP240				MP125				MP136		MP166		MP168				MP192		MP285	
	Core	Rim	Core	Core	Core	Rim	Core	Rim	Core	Rim	Core	Rim	Core	Rim	Core	Rim	Core	Rim	Core	Rim	Core	Rim	Core	Rim	Core	Rim	Core	Rim
SiO_2	50.6	51.3	51.6	51.7	51.0	52.7	51.7	52.5	51.5	52.1	51.9	51.5	53.2	52.4	51.20	52.64	53.5	52.2	51.6	52.2	52.4	52.4	51.8	51.7	52.7	53.1	51.5	50.0
TiO_2	0.74	0.71	0.72	0.87	1.26	0.75	0.72	0.54	0.87	0.58	0.70	0.71	0.21	0.48	0.84	0.64	0.36	0.45	0.72	0.68	0.63	0.72	0.71	0.71	0.58	0.57	0.55	0.76
Al_2O_3	3.5	2.8	3.4	3.3	3.4	2.9	3.9	3.1	3.5	2.8	3.2	3.2	1.2	2.4	3.5	2.7	1.9	3.0	3.0	2.7	3.0	2.9	3.1	3.0	2.9	3.1	3.3	4.1
Cr_2O_3	0.19	0.23	0.76	0.33	0.96	0.13	0.65	0.45	0.38	0.45	0.37	0.42	0.16	0.24	0.41	0.26	0.33	0.47	0.21	0.25	0.26	0.14	0.23	0.23	0.24	0.24	0.58	1.77
Fe_2O_3	1.89	1.85	1.01	0.39	0.70	0.65	0.81	0.65	1.13	0.54	0.58	2.02	1.53	1.26	1.79	0.30	0.00	0.33	1.78	0.06	0.00	0.00	0.83	1.13	0.00	0.00	0.34	1.81
FeO	3.9	3.3	5.0	5.0	5.4	4.3	3.9	4.4	3.7	4.1	4.5	2.9	3.4	3.8	3.4	5.0	4.7	5.1	4.2	5.6	5.3	5.3	4.4	4.5	5.0	5.4	5.1	3.9
MnO	0.19	0.14	0.18	0.17	0.20	0.15	0.14	0.19	0.16	0.19	0.18	0.17	0.20	0.19	0.21	0.26	0.18	0.18	0.19	0.21	0.15	0.14	0.16	0.20	0.18	0.17	0.16	0.21
MgO	15.8	15.3	14.6	14.9	14.9	15.7	15.0	15.2	15.3	15.2	16.0	15.8	16.0	15.5	15.3	15.2	16.0	15.2	15.1	15.4	16.3	16.2	15.9	15.5	15.4	15.0	15.6	15.0
CaO	21.2	23.1	22.3	22.6	22.0	23.2	22.8	23.0	22.6	23.3	21.6	22.5	23.4	23.2	22.5	22.8	22.5	22.3	22.7	22.0	20.8	21.0	22.0	22.3	21.6	22.0	21.5	22.0
Na_2O	0.36	0.37	0.56	0.41	0.39	0.32	0.54	0.45	0.46	0.35	0.39	0.46	0.29	0.38	0.49	0.43	0.21	0.39	0.44	0.35	0.32	0.29	0.34	0.35	0.56	0.42	0.32	0.31
Total	98.3	99.2	100.1	99.7	100.3	101.0	100.2	100.5	99.6	99.5	99.3	99.7	99.9	99.8	99.68	100.16	99.7	99.6	99.8	99.4	99.0	99.1	99.4	99.6	99.2	100.1	98.9	99.9
Si	1.887	1.902	1.901	1.909	1.882	1.916	1.894	1.919	1.895	1.922	1.912	1.895	1.956	1.927	1.887	1.932	1.962	1.926	1.903	1.930	1.931	1.934	1.910	1.909	1.946	1.944	1.912	1.850
Ti	0.021	0.020	0.020	0.024	0.035	0.020	0.020	0.015	0.024	0.016	0.019	0.020	0.006	0.013	0.023	0.018	0.010	0.012	0.020	0.019	0.018	0.020	0.020	0.020	0.016	0.016	0.015	0.021
Al^{IV}	0.113	0.098	0.099	0.091	0.118	0.084	0.106	0.081	0.105	0.078	0.088	0.105	0.044	0.073	0.113	0.068	0.038	0.074	0.097	0.070	0.069	0.066	0.090	0.091	0.054	0.056	0.088	0.150
Al^{VI}	0.040	0.026	0.049	0.051	0.029	0.044	0.064	0.052	0.047	0.042	0.050	0.032	0.007	0.031	0.040	0.048	0.045	0.054	0.032	0.048	0.062	0.058	0.045	0.039	0.070	0.079	0.054	0.029
Cr	0.006	0.007	0.022	0.010	0.028	0.004	0.019	0.013	0.011	0.013	0.011	0.012	0.005	0.007	0.012	0.007	0.010	0.014	0.006	0.007	0.007	0.004	0.007	0.007	0.007	0.007	0.017	0.052
Fe^{3+}	0.053	0.052	0.028	0.011	0.020	0.018	0.022	0.018	0.031	0.015	0.016	0.056	0.042	0.035	0.050	0.008	0.000	0.009	0.049	0.002	0.000	0.000	0.023	0.031	0.000	0.000	0.009	0.050
Fe^{2+}	0.122	0.103	0.153	0.154	0.166	0.131	0.120	0.134	0.114	0.127	0.138	0.089	0.103	0.116	0.105	0.153	0.145	0.157	0.128	0.171	0.163	0.164	0.134	0.139	0.155	0.166	0.158	0.121
Mn	0.006	0.004	0.006	0.005	0.006	0.005	0.004	0.006	0.005	0.006	0.006	0.005	0.006	0.006	0.007	0.008	0.006	0.006	0.006	0.007	0.005	0.004	0.005	0.006	0.006	0.005	0.005	0.006
Mg	0.880	0.844	0.803	0.820	0.820	0.851	0.821	0.830	0.842	0.834	0.881	0.865	0.877	0.850	0.838	0.830	0.875	0.838	0.831	0.849	0.896	0.892	0.874	0.850	0.849	0.821	0.863	0.824
Ca	0.847	0.919	0.880	0.895	0.868	0.904	0.892	0.900	0.893	0.921	0.851	0.887	0.934	0.914	0.890	0.897	0.886	0.882	0.896	0.872	0.820	0.829	0.869	0.882	0.855	0.861	0.854	0.873
Na	0.026	0.026	0.040	0.029	0.028	0.023	0.039	0.032	0.033	0.025	0.028	0.033	0.021	0.027	0.035	0.031	0.015	0.028	0.031	0.025	0.023	0.021	0.024	0.025	0.028	0.030	0.023	0.022
Wo	45.8	49.2	47.9	47.9	46.8	47.9	48.7	48.3	48.3	48.9	45.5	48.2	48.8	48.6	48.55	47.71	46.5	47.0	48.3	46.1	43.7	44.0	46.3	47.1	46.0	46.6	45.6	48.0
En	47.6	45.2	43.7	43.9	44.2	45.1	44.8	44.5	45.5	44.3	47.1	47.0	45.8	45.2	45.72	44.15	45.9	44.6	44.8	44.9	47.7	47.3	46.6	45.4	45.7	44.4	46.0	45.3
Fs	6.6	5.5	8.3	8.2	9.0	6.9	6.5	7.2	6.2	6.8	7.4	4.8	5.4	6.2	5.73	8.14	7.6	8.4	6.9	9.1	8.7	8.7	7.1	7.4	8.3	9.0	8.4	6.6
Mg#	87.8	89.1	84.0	84.2	83.2	86.7	87.3	86.1	88.1	86.8	86.4	90.7	89.5	88.0	88.9	84.4	85.8	84.2	86.6	83.2	84.6	84.5	86.7	85.9	84.6	83.2	84.5	87.2

Structural formula based on 4 cations and 6 oxygens, (n.d.): not determined. Measurements were made on a Cameca SX50 electron microprobe at 15 kV and 20 nA.

Table 3
Representative major-element compositions of plagioclases from plg-wehrlites, troctolite, ol- and cpx-gabbros and anorthosite

Rock types	Plg-wehrlites				Troctolite		Ol-gabbros								Cpx-gabbros		Anorthosite	
Sample numbers	MP106		FB1095		MP240		MP125		MP136		MP166		FB1091		MP168		MP285	
	Core	Rim	Core	Rim	Core	Rim	Core	Rim	Core	Rim	Core	Rim	Core	Rim	Core	Rim	Core	Rim
SiO_2	52.1	50.5	50.6	51.2	49.2	49.2	49.6	49.6	47.1	49.3	50.0	49.8	51.5	52.0	48.3	48.7	49.2	48.6
Al_2O_3	30.0	30.4	31.0	30.5	32.3	32.3	31.4	31.5	33.5	32.0	31.3	31.5	31.3	30.8	32.0	31.8	31.7	32.7
Fe_2O_3	0.23	1.35	0.18	0.20	0.12	0.11	0.23	0.22	0.10	0.13	0.25	0.23	0.13	0.17	0.15	0.16	0.02	0.15
MgO	0.01	0.44	0.00	0.00	0.01	0.00	0.01	0.02	0.00	0.00	0.00	0.00	0.01	0.00	0.00	0.00	0.01	0.01
CaO	12.8	12.8	14.2	13.5	15.5	15.6	14.7	14.8	16.6	15.0	14.8	14.5	13.8	13.6	14.8	14.7	14.9	15.4
Na_2O	4.10	3.63	3.46	3.67	2.89	2.94	3.02	3.18	1.92	2.94	2.89	3.17	3.29	3.70	3.04	3.00	3.04	2.71
K_2O	0.04	0.03	0.05	0.07	0.01	0.03	0.04	0.04	0.00	0.01	0.06	0.08	0.38	0.39	0.02	0.01	0.07	0.03
Total	99.30	99.10	99.45	99.16	100.02	100.16	98.95	99.33	99.15	99.33	99.44	99.34	100.35	100.62	98.25	98.40	98.95	99.58
Si	2.379	2.320	2.315	2.345	2.247	2.247	2.284	2.280	2.177	2.263	2.293	2.285	2.330	2.349	2.245	2.257	2.268	2.229
Al^{IV}	1.614	1.644	1.674	1.648	1.740	1.737	1.703	1.704	1.822	1.733	1.693	1.706	1.673	1.640	1.751	1.740	1.725	1.771
Al^{VI}	0.000	0.000	0.000	0.000	0.000	0.000	0.000	0.000	0.000	0.000	0.000	0.000	0.000	0.000	0.000	0.000	0.000	0.000
Fe^{3+}	0.008	0.047	0.006	0.007	0.004	0.004	0.008	0.008	0.003	0.004	0.009	0.008	0.004	0.006	0.005	0.006	0.001	0.005
Mg	0.001	0.030	0.000	0.000	0.001	0.000	0.000	0.001	0.000	0.000	0.000	0.000	0.001	0.000	0.000	0.000	0.001	0.001
Ca	0.625	0.631	0.695	0.663	0.759	0.761	0.728	0.728	0.821	0.737	0.724	0.715	0.668	0.659	0.736	0.731	0.737	0.755
Na	0.363	0.323	0.307	0.326	0.256	0.260	0.270	0.283	0.172	0.261	0.256	0.282	0.289	0.324	0.274	0.270	0.272	0.241
K	0.002	0.002	0.003	0.004	0.001	0.002	0.002	0.002	0.000	0.000	0.004	0.005	0.022	0.022	0.001	0.001	0.004	0.002
Ab	36.6	33.8	30.5	32.8	25.2	25.5	27.0	27.9	17.4	26.2	26.1	28.2	29.5	32.2	27.1	26.9	26.8	24.1
An	63.1	66.0	69.2	66.8	74.7	74.4	72.8	71.8	82.6	73.8	73.6	71.4	68.3	65.6	72.8	73.0	72.8	75.7
Or	0.2	0.2	0.3	0.4	0.1	0.2	0.2	0.2	0.0	0.0	0.4	0.5	2.2	2.2	0.1	0.1	0.4	0.2

Structural formula based on 8 oxygens. Measurements were made on a Cameca SX50 electron microprobe at 15 kV and 10 nA.

Table 4
Representative major-element compositions of amphiboles from wehrlites, plg-wehrlites, troctolite, ol- and cpx-gabbros and anorthosite

Rock types	Wehrlite	Plg-wehrlite		Troctolite		Ol-gabbros					Cpx-gabbros			Anorthosite
Sample numbers	MP243	FB1095		MP240		MP125		MP136	MP166		MP168	MP192		MP285
SiO_2	42.5	43.3	43.1	43.1	44.6	42.4	42.6	51.0	41.9	42.6	42.9	43.3	42.5	46.3
TiO_2	1.80	0.03	2.13	1.44	1.09	0.02	0.15	0.61	2.33	2.42	3.68	2.37	3.53	1.58
Al_2O_3	13.8	16.0	13.3	14.5	13.3	17.1	15.8	5.9	13.6	12.8	12.0	13.2	12.8	10.9
Cr_2O_3	0.15	0.00	0.09	0.17	0.13	0.03	0.09	0.26	0.10	0.11	0.27	0.12	0.18	0.07
Fe_2O_3	1.3	6.5	3.2	4.5	4.0	6.8	8.4	3.1	3.7	4.5	2.1	2.5	1.9	2.6
FeO	7.2	1.5	4.5	2.9	3.7	1.8	0.7	6.3	6.3	5.8	7.8	6.5	6.8	7.5
MnO	0.06	0.19	0.14	0.05	0.16	0.10	0.14	0.19	0.06	0.13	0.09	0.10	0.11	0.21
MgO	15.4	15.7	16.1	16.1	16.0	15.0	15.6	17.0	14.3	14.5	14.3	14.7	14.7	14.3
CaO	11.9	11.8	12.2	12.2	12.1	12.2	11.9	12.7	12.0	11.8	12.0	11.9	11.9	12.0
Na_2O	2.50	2.55	2.46	2.31	2.19	2.27	2.30	0.67	1.86	1.88	1.76	2.30	2.05	1.06
K_2O	n.d.	0.66	0.92	0.58	0.50	0.37	0.58	0.10	1.21	1.11	1.16	0.77	1.03	0.74
OH	2.01	2.12	2.09	2.10	2.11	2.62	2.51	2.12	2.06	2.07	2.07	2.08	2.07	2.08
Total	99.5	100.5	100.2	99.9	99.8	100.7	100.8	100.1	99.4	99.7	100.1	99.88	99.5	99.2
Si	6.338	6.114	6.173	6.148	6.355	6.016	6.038	7.226	6.112	6.187	6.226	6.250	6.176	6.685
Al^{IV}	1.662	1.886	1.827	1.852	1.645	1.984	1.962	0.774	1.888	1.813	1.774	1.750	1.824	1.315
Al^{VI}	0.756	0.786	0.426	0.579	0.584	0.868	0.680	0.218	0.455	0.382	0.280	0.497	0.370	0.534
Ti	0.202	0.003	0.229	0.154	0.117	0.002	0.016	0.065	0.256	0.264	0.402	0.257	0.385	0.172
Cr	0.018	0.000	0.010	0.019	0.015	0.004	0.011	0.029	0.012	0.013	0.032	0.014	0.020	0.008
Fe^{3+}	1.051	0.696	0.350	0.487	0.433	0.727	0.897	0.332	0.404	0.490	0.227	0.267	0.207	0.282
Fe^{2+}	0.000	0.178	0.538	0.344	0.437	0.210	0.082	0.742	0.765	0.705	0.944	0.784	0.820	0.905
Mn	0.008	0.022	0.017	0.006	0.019	0.012	0.016	0.023	0.007	0.016	0.011	0.012	0.014	0.026
Mg	3.426	3.315	3.430	3.410	3.395	3.177	3.298	3.592	3.101	3.129	3.104	3.171	3.184	3.073
Ca	1.897	1.790	1.866	1.857	1.842	1.846	1.804	1.932	1.877	1.832	1.861	1.837	1.845	1.857
Na	0.722	0.699	0.684	0.638	0.605	0.624	0.630	0.183	0.526	0.529	0.494	0.643	0.576	0.297
K	n.d.	0.119	0.168	0.105	0.091	0.066	0.104	0.018	0.225	0.206	0.215	0.142	0.191	0.136
OH*	2	2	2	2	2	2	2	2	2	2	2	2	2	2
Total cations	16.08	15.61	15.72	15.60	15.54	15.54	15.54	15.13	15.63	15.57	15.57	15.62	15.61	15.29
Amphibole names	magnesio-hastingsitic-hornblende	pargasite	pargasite	pargasite	pargasitic hornblende	pargasite	magnesio-hastingsite	magnesio-hastingsite	titanian-pargasite	titanian-magnesio-hastingsite	titanian-pargasite	titanian-pargasite	titanian-pargasite	magnesio-hornblende

Structural formula based on 23 equivalent oxygens. Measurements were made on a Cameca SX50 electron microprobe at 15 kV and 10 nA. Amphibole names after Leake et al. (1997).

Table 5
Trace-element compositions of clinopyroxene, plagioclase and amphibole used in the in-situ crystallization modeling

Rock types	Wehrlite	Plg-wehrlite			Troctolite			Ol-gabbros								Cpx-gabbro			Anorthosite		
Sample numbers	MP243	MP106			MP240			MP125		MP136			MP166			MP168			MP285		
Mineral types	cpx	cpx	plg	amph	cpx	plg	amph	cpx	plg	cpx	plg	amph	cpx	plg	amph	cpx	plg	amph	cpx	plg	amph
Rb	0.05	0.09	2	16	0.27	<0.1	8	0.16	<0.02	0.09	0.17	13	0.80	<0.04	16	0.07	0.02	12	0.15	0.18	61
Ba	2	1	81	132	0.3	42	63	0.6	43	1	38	98	0.1	47	60	0.7	45	81	2	47	8
Th	0.24	0.37	<0.03	1.13	0.32	<0.00	0.38	0.48	0.14	0.48	0.04	1.14	0.88	<0.03	2.47	0.29	<0.00	0.62	0.22	<0.03	0.71
Nb	<0.05	0.06	<0.18	20.38	<0.04	<0.05	8.21	<0.04	<0.02	<0.05	<0.06	28.27	<0.04	<0.05	16.72	<0.04	<0.08	8.78	0.22	<0.04	12.06
Ta	<0.01	<0.01	<0.11	1.48	<0.01	<0.05	0.72	<0.01	<0.05	<0.01	<0.00	1.54	<0.01	<0.02	1.03	<0.01	<0.00	0.67	0.08	<0.03	0.56
Pb	0.16	0.18	2.9	1.35	0.07	1.3	0.49	0.13	1.1	0.12	2.0	0.94	0.29	1.3	0.61	0.09	1.15	0.40	<0.02	1.3	0.45
Sr	32	27	1054	171	31	793	101	38	837	29	880	214	35	909	102	33	877	147	25	855	97
Zr	22	49	<0.45	223	20	0.1	65	19	0.8	26	0.1	174	22	<0.06	173	23	<0.00	99	32	<0.09	150
Hf	0.97	1.23	0.11	7.31	0.87	<0.09	1.92	0.93	<0.08	0.80	<0.14	6.04	0.85	<0.00	4.28	1.01	<0.22	3.51	1.09	<0.22	3.11
Ti	4252	4618	48	21612	4287	383	11908	3897	–	2998	–	4563	4376	168	14735	2815	–	13957	5190	143	16680
Y	18	24	0.3	67	17	0.3	21	15	0.9	16	0.2	45	17	0.1	29	18	<0.23	47	19	0.2	31
K	–	75	855	8117	36	398	5212	–	275	–	111	1477	–	501	9340	–	363	7230	163	605	6008
La	2.00	3.02	3.68	12.32	1.39	1.68	2.81	1.73	2.43	1.56	3.42	8.06	1.86	3.05	6.81	1.91	2.87	6.77	1.24	2.81	5.10
Ce	6.56	10.67	5.95	36.65	5.98	3.14	13.08	6.40	3.27	6.79	5.40	29.78	7.72	4.86	24.48	7.82	4.77	21.79	7.22	4.91	23.14
Pr	1.41	2.09	0.55	6.13	1.13	0.37	2.55	1.27	0.49	1.47	0.46	5.59	1.41	0.42	4.26	1.50	0.49	4.15	1.68	0.51	4.20
Nd	8.08	11.06	1.93	33.71	6.59	1.49	13.87	7.56	1.63	8.09	1.50	28.73	8.05	1.25	23.41	9.13	1.60	24.58	8.48	1.71	22.88
Sm	2.62	3.36	0.19	10.17	2.28	0.21	5.00	2.60	0.32	2.70	0.22	8.39	2.88	0.19	7.19	3.14	0.24	8.28	2.99	0.24	6.32
Eu	0.83	0.85	0.41	2.60	0.69	0.54	1.80	0.69	0.55	0.77	0.53	2.30	0.90	0.56	2.20	0.84	0.68	2.28	0.83	0.48	1.98
Gd	3.22	3.79	0.22	11.80	2.65	0.25	4.91	2.77	0.12	2.86	0.17	8.38	2.95	0.05	6.99	3.22	0.18	9.26	3.53	0.16	6.45
Tb	0.54	0.69	<0.07	2.00	0.45	<0.04	0.67	0.56	<0.03	0.59	<0.01	1.45	0.49	<0.02	1.18	0.60	<0.06	1.61	0.66	0.03	0.99
Dy	3.66	4.53	<0.17	11.84	2.95	<0.12	4.71	2.83	0.06	3.31	0.06	8.61	3.13	<0.08	7.45	3.78	<0.28	9.19	3.41	0.10	6.30
Ho	0.77	0.98	<0.04	2.41	0.46	<0.00	0.82	0.52	<0.06	0.74	<0.06	1.59	0.67	<0.03	1.51	0.77	<0.00	1.82	0.75	<0.03	1.16
Er	1.78	2.58	<0.21	6.74	1.54	<0.09	2.14	1.66	<0.15	1.74	<0.07	4.33	1.90	<0.00	3.91	1.97	<0.09	4.99	2.02	<0.09	3.54
Yb	1.40	2.29	<0.38	5.41	1.57	<0.16	1.78	1.43	<0.23	1.66	<0.35	3.20	1.54	<0.00	3.12	1.78	<0.00	4.42	1.85	<0.00	3.61
Lu	0.19	0.31	<0.09	0.77	0.18	<0.04	0.23	0.18	<0.11	0.23	<0.00	0.63	0.22	<0.02	0.41	0.23	<0.03	0.68	0.23	<0.03	0.38

(–): not determined. Measurements by LA-ICPMS.

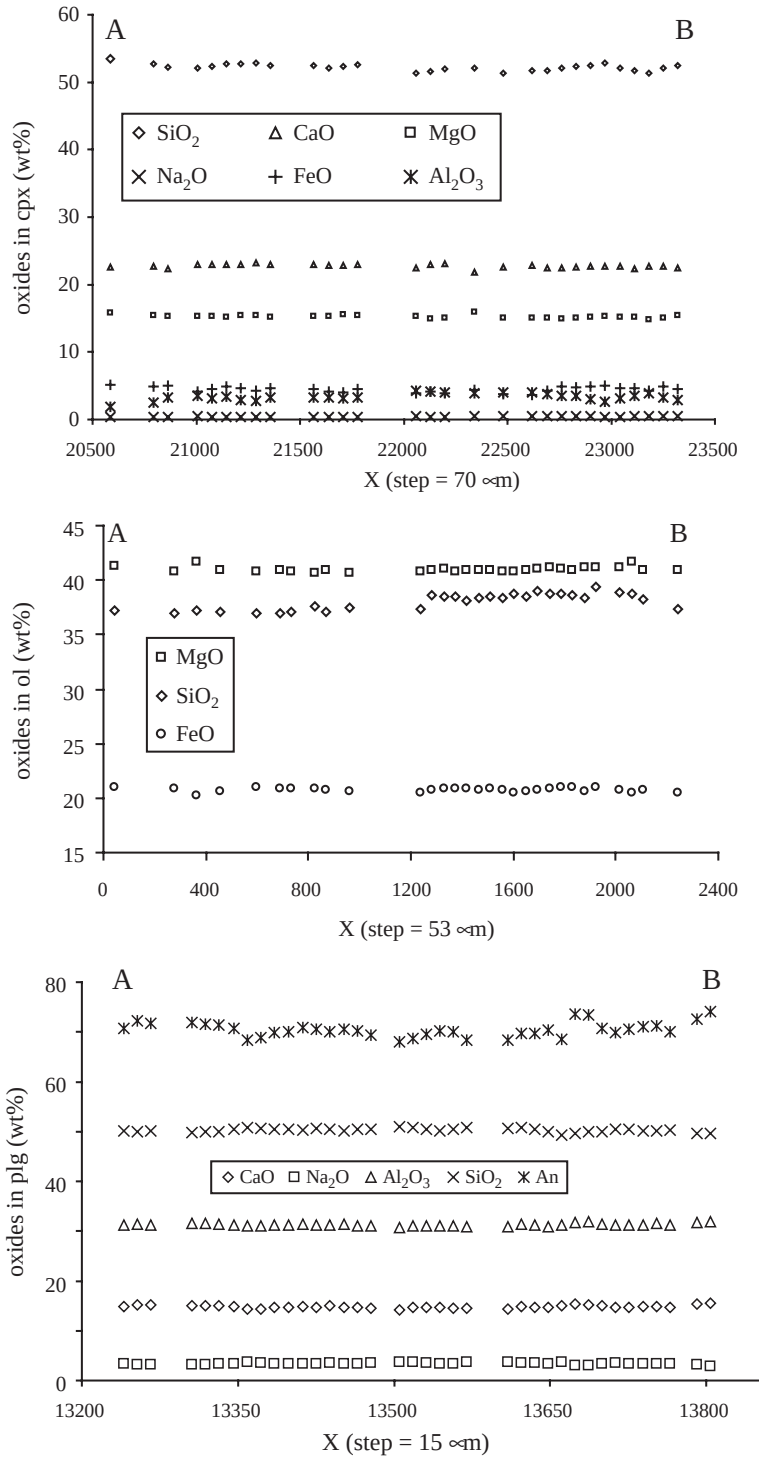

Fig. 4. Profiles showing the lack of variations of major elements along minerals (olivine=ol, clinopyroxene=cpx and plagioclase=plg). Measurements were made on a Cameca SX50 electron microprobe (see analytical procedures).

Troctolites are medium-grained adcumulates, consisting of anhedral olivine (35 vol.%; Fo = 78.7–79.4) and euhedral, variable sized laths of bytownitic plagioclase (65 vol.%, An_{74}), underlying the cumulative texture of the rock. Clinopyroxene is scarce and frequently absent at the thin section scale (<3%). It is diopsidic (mean of 9 analyses: $En_{45.5}Fs_{6.5}Wo_{48}$); the CaO content increases systematically from core (>21.6 wt.%) to rim (maximum 23.3 wt.%). Al_2O_3 ranges from 3.2 to 3.5 wt.%, but does not present coherent variations between core and rim. Na_2O remains constant close to 0.3 wt.%. Rare magnesio-hornblende fills the interstices between plagioclases.

Olivine gabbros display a typical adcumulate texture. Modal proportions of cumulus phases are slightly variable and plagioclase is generally dominant. Olivine is anhedral and displays a more homogeneous composition (Fo = 76.4–79.4) than in plagioclase-wehrlites, but similar Ni contents. MnO is rather constant with mean concentrations close to 0.3 wt.%. Diopside crystallizes as euhedral to anhedral grains of variable size, indicating an early-stage magmatic crystallization. $Mg\#_{cpx}$ ranges from 84 to 89 and remains rather constant between core and rim. CaO content shows limited variations ($22.0 < CaO < 23.4$). Clinopyroxene is characterized by a wide range in Al content, which is rather low ($1.2 < Al_2O_3 < 3.5$ wt.%). Na_2O (0.21 to 0.49 wt.%) is positively correlated with Al_2O_3 as does TiO_2. Plagioclase is tabular and preferentially oriented in the layering plane. It is chemically zoned with bytownitic cores (up to $An_{82.6}$) and labradoritic rims ($An_{65.6}$). Magmatic amphibole (Ti-rich pargasite, magnesio-hastingsite or magnesio-hornblende) occurs as interstitial phase between plagioclase and/or clinopyroxene or patches riming clinopyroxene. Its distribution is not spatially uniform at the scale of a thin section. The Al^{VI} content is anticorrelated with Ti. Their Mg# is the highest observed in all Mont Collon cumulates.

Olivine-free **clinopyroxene gabbros** are essentially composed of euhedral cumulitic clinopyroxene and plagioclase, in equal proportions, showing preferred orientation. Clinopyroxene is diopsidic and characterized by low Al_2O_3 (<3.1 wt.%) and Na_2O (0.29 to 0.56 wt.%) contents. Rim is generally depleted in Al_2O_3 and TiO_2 with respect to the core. It displays relatively constant $Mg\#_{cpx}$ close to 85. Plagioclase crystallizes as equigranular crystals and exhibits commonly unzoned bytownitic composition (An_{73}). A variable amount (up to 8%) of intercumulus magmatic amphibole (Ti-rich pargasite) surrounds the clinopyroxene and/or oxides. Its Mg# is the lowest among magmatic amphiboles in the massif.

The unique **anorthositic layer** observed in the Dents de Bertol area is essentially constituted of tabular grains of unzoned bytownitic plagioclase without preferential orientation; although a weak fabric is visible at the outcrop scale. There is also a small amount of diopsidic clinopyroxene (4–5 vol.%) and amphibole (<1 vol.%), which is commonly a magnesio-hornblende with relatively high TiO_2 content (up to 1.58 wt.%).

The **pegmatitic gabbros** have well-preserved magmatic textures, although they are partly recrystallized under greenschist facies conditions. They consist of large crystals (up to several cm long) of plagioclase and pale green polycrystalline secondary amphibole.

4. Mineral evolution in the cumulitic sequence

The crystallization sequence in the mafic cumulates of the Mont Collon intrusion is ambiguous. Olivine is the first phase to appear, followed either by plagioclase or clinopyroxene (e.g. in troctolites and wehrlites, respectively) depending on the lithologies and probably the location within the magma chamber (i.e. variation in space and time of parameters such as P_{H2O}, fO_2, magma replenishment). Ilmenite and/or magnetite crystallize subsequently and are mostly associated with Ti-amphibole, which is the last phase to form. Mineral compositions are surprisingly homogeneous among the different rock types (see profiles in minerals in Fig. 4). The most primitive olivine composition (Fo = 78.7–79.4) is found in the troctolites, but it is barely different in other lithologies (Fo = 74–77). The overall plagioclase compositional range is $An_{83–63}$, not much larger than zoning in individual crystals in olivine-gabbros ($An_{83–65}$). Clinopyroxene is diopsidic, but shows some weak elemental variation in plagioclase-wehrlites, where less calcic composition (endiopside–augite joint) are locally found in crystal cores (by 0.1–0.5 wt.% CaO). Aluminum exhibits larger variations; the Al_2O_3 content of clinopyroxene ranges from 1 to 5 wt.% over the pluton, with up to 1

wt.% Al_2O_3 increase (in plagioclase-wehrlites) or decrease (in clinopyroxene-gabbros) between core and rim within a single clinopyroxene crystal and up to 2 wt.% within a sample. Small-scale variations probably reflect fluctuation in the silica activity of the melt (Deer et al., 1992) in the vicinity of crystallizing grains in relation with the nature of surrounding phases. Composition of interstitial amphibole does not vary significantly, except for its Ti content (from 0 to 3.5 wt.% TiO_2 over the massif), which is in direct relationship with the presence or absence of ilmenite/magnetite in the sample.

5. Thermo-barometric conditions of emplacement of the Mont Collon complex

Geothermo-barometric calculations were made on olivine- and clinopyroxene-bearing samples, whose modeled interstitial liquid proportion (L, see later section) was minimal in order to minimize late- to post-solidus chemical re-equilibration effects between mineral phases. We used the geothermometer of Loucks (1996) based on the Fe–Mg exchange between augite and olivine, applicable to mineral assemblages including olivine + augite + plagioclase ± pigeonite or orthopyroxene over a wide range of pressure (up to 1 GPa). Temperature was extracted from Loucks equation using Wolfran© Mathematica© software. It ranges from 1070 to 1120 ± 6 °C. These temperatures seem reasonable for a cotectic precipitation of olivine + plagioclase + clinopyroxene from a water-bearing basaltic magma. Reporting these values into the Nimis and Ulmer (1998) clinopyroxene geobarometer yields pressures between 0.5 and 0.7 GPa, which points to a mid-crustal level of intrusion. As this geobarometer is highly sensitive to T and, to a lesser extent, to magma composition and water content, the obtained pressures must be considered as first-order approximation. A moderate pressure of crystallization is also supported by the absence of orthopyroxene as an early crystallizing phase and by the widespread presence of olivine + plagioclase in most cumulates (i.e. <0.5 GPa according to Green and Ringwood, 1967). This is also consistent with the low Al_2O_3 (<4.1 wt.%) and Na_2O (<0.56 wt.%) contents of clinopyroxene, and the relatively high An content of plagioclase (up to 82.6), although the latter could rather be related to the presence of water in the magma. Calculations were also performed on the interstitial magmatic amphibole using the amphibole/plagioclase geothermometer B of Holland and Blundy (1994), applicable to silica-undersaturated rocks in the 400–1000 °C and 0.1 to 1.5 GPa range. We obtained temperatures of about 740 ± 40 °C for a pressure of 0.5 GPa. This value must be very close to the solidus temperature of the system at 0.5 GPa, according to experimental work on partial melting of (meta)basalts and gabbros at $P_{H2O} < P_{tot}$ (Holloway and Burnham, 1972; Springer and Seck, 1997). Temperature calculations were also made on coronitic amphiboles using the same geothermometer; results (700 ± 40 °C at 0.5 GPa) are close to temperatures calculated for the interstitial magmatic amphiboles, which means that coronitic reactions occurred at subsolidus conditions.

6. Whole-rock major- and minor element chemistry

Chemical data are reported in Tables 6a and 6b. Major- and trace-element distributions are illustrated in Figs. 5–8 as well as in Fig. 9 for the specific chemical evolution of the Dents de Bertol cumulative sequence. Iron is recalculated as total iron (FeO*) following the recommendations of Irvine and Baragar (1971). CIPW norm calculation has been restricted to unmetamorphosed samples, as it is very sensitive to potentially mobile elements such as Na and K during metamorphism or alteration processes. Rocks are olivine and hypersthene normative and plot in the olivine tholeiite field (Ol–Hy–Di triangle) of the Ne–Di–Ol–Hy–Q diagram of Thompson (1984).

Notes to Table 6a

Major-elements and some traces determined by X-ray fluorescence (XRF). (–): not determined. Other trace elements measured on a Fisons VG PlasmaQuad + ICPMS.

[a] XRF trace-element analysis using classical short measurement time procedure (15 min).

[b] XRF analysis using long measurement time procedure (180 min).

Table 6a
Selected whole-rock major- and trace-element compositions (wehrlites, plg-wehrlites, troctolite, ol- and cpx-gabbros, pegmatitic gabbros and anorthosite)

Rock type	Wehrlites				Plg-wehrlites		Ol-gabbros					
Sampling area	DB	CP	DB	DB	scree MC	scree MC	scree MC	DB	DB	DB	DB	DB
Stratigraphic mark (m)	306				FB1095	MP106		15	30	40	85	105
Sample number	MP155	MP213	MP243	MP278			FB1091	MP123	MP125	MP127	MP135	MP136
SiO_2	45.8	40.3	40.1	41.5	44.8	45.7	46.8	47.9	46.4	47.9	48.5	47.6
TiO_2	0.36	0.33	0.20	0.58	0.37	0.54	0.37	0.36	0.26	0.34	0.36	0.28
Al_2O_3	11.2	4.2	7.2	9.7	12.2	10.6	15.3	16.5	19.3	17.8	19.2	19.5
FeO[a]	8.6	15.9	14.2	11.6	10.7	9.9	7.3	5.1	5.2	5.3	4.4	4.5
MnO	0.15	0.14	0.19	0.16	0.16	0.17	0.12	0.10	0.09	0.09	0.08	0.08
MgO	16.7	27.4	24.2	21.6	18.1	15.5	13.5	10.3	10.0	10.0	8.3	8.6
CaO	13.6	2.4	6.0	7.6	9.5	13.2	12.4	14.8	13.2	14.1	15.1	14.2
Na_2O	0.84	0.00	0.19	0.33	1.21	1.28	1.65	1.63	1.90	1.69	1.88	1.88
K_2O	0.08	0.06	0.05	0.11	0.14	0.17	0.18	0.16	0.25	0.17	0.20	0.20
P_2O_5	0.02	0.04	0.03	0.10	0.04	0.04	0.05	0.03	0.04	0.04	0.04	0.03
LOI	2.7	8.7	7.4	6.1	2.1	1.8	1.6	2.0	2.5	2.2	1.5	2.2
Total	100.2	99.5	99.8	99.5	99.3	99.2	99.2	99.0	99.1	99.6	99.6	99.1
Mg#	77.5	75.5	75.3	76.8	75.1	73.5	76.9	78.1	77.2	77.2	77.2	77.4
in ppm												
Cu[a]	49	–	14	–	15	83	15	–	15	567	405	31
S[a]	573	–	78	–	–	5823	40	–	992	6022	4717	1058
Sc[a]	86	–	–	–	62	97	50	–	34	35	27	27
V[b]	132	59	74	90	74	165	91	–	87	117	131	106
Cr[b]	1048	110	270	793	390	1574	283	–	390	532	405	375
Ni[b]	141	191	161	287	244	250	91	–	45	39	62	60
Ga[b]	11	7	9	10	12	13	13	–	15	15	15	15
Zn[b]	59	97	57	82	85	62	49	–	36	38	30	35
Zr[b]	26	36	15	33	37	48	42	–	36	41	40	35
Co	74	113	103	100	74	63	53	–	47	35	32	43
Cs	0.32	0.26	0.44	0.43	0.32	0.40	0.84	–	0.23	0.13	0.20	0.15
Rb	3.0	2.4	1.3	2.5	3.0	4.1	4.3	–	6.6	3.2	3.9	5.4
Ba	29.3	7.6	5.7	21.7	29.3	39.2	34.7	–	53.2	36.1	43.8	45.7
Th	0.36	0.69	0.04	0.14	0.36	0.28	0.31	–	0.30	0.38	0.39	0.53
U	0.09	0.15	0.03	0.04	0.09	0.05	0.08	–	0.06	0.09	0.08	0.15
Nb	0.82	2.17	0.26	2.31	0.82	1.09	0.93	–	0.94	0.82	0.76	0.79
Ta	0.06	0.14	0.15	0.12	0.06	0.07	0.06	–	0.28	0.05	0.04	0.27
Pb	1.21	0.54	0.94	1.01	1.21	1.01	1.01	–	1.03	1.44	0.99	1.76
Sr	308.8	14.7	110.9	195.8	308.8	278.4	400.8	–	621.7	473.7	502.1	558.5
Hf	0.60	0.59	0.41	0.74	0.60	1.17	0.69	–	0.49	0.67	0.66	0.69
Y	6.8	8.2	5.8	11.9	6.8	15.7	8.5	–	6.5	8.9	9.3	8.3
La	2.64	1.66	1.37	2.93	2.64	3.56	2.85	–	2.75	3.18	3.02	3.15
Ce	6.17	4.97	3.19	8.57	6.17	10.10	6.84	–	6.28	7.65	7.32	7.46
Pr	0.88	0.82	0.50	1.43	0.88	1.63	1.01	–	0.91	1.12	1.11	1.08
Nd	3.99	4.01	2.70	7.20	3.99	8.05	4.81	–	4.06	5.15	5.38	4.99
Sm	1.03	1.19	0.69	1.98	1.03	2.40	1.32	–	1.07	1.44	1.49	1.43
Eu	0.51	0.15	0.37	0.55	0.51	0.79	0.59	–	0.62	0.68	0.72	0.70
Gd	1.19	1.37	0.97	2.12	1.19	2.73	1.49	–	1.17	1.63	1.70	1.53
Tb	0.20	0.24	0.18	0.34	0.20	0.45	0.24	–	0.19	0.26	0.27	0.25
Dy	1.17	1.38	1.13	1.99	1.17	2.81	1.47	–	1.11	1.58	1.62	1.49
Ho	0.25	0.29	0.21	0.40	0.25	0.58	0.30	–	0.22	0.32	0.33	0.28
Er	0.69	0.77	0.66	1.10	0.69	1.62	0.83	–	0.60	0.87	0.91	0.74
Yb	0.59	0.66	0.51	0.85	0.59	1.32	0.68	–	0.52	0.72	0.72	0.65
Lu	0.09	0.09	0.08	0.13	0.09	0.19	0.10	–	0.07	0.10	0.10	0.09

DB	DB	DB	DB	DB	DB	DB	DB	DB	DB	MC	DB	DB	DB	DB
238	243	308	310	312.5	317	320	330.5	334.5	335.5	427	490	500	515	520
MP150	MP152	MP156	MP157	MP159	MP160	MP161	MP164	MP166	MP167	MP176	MP181	MP188	MP189	MP191
46.9	44.8	47.4	46.5	47.2	47.7	45.3	45.9	46.0	46.5	47.5	47.4	47.2	43.8	43.8
0.23	0.15	0.30	0.32	0.29	0.27	0.21	0.22	0.23	0.25	0.29	0.46	0.27	0.16	0.23
23.1	19.8	18.9	14.2	18.2	20.1	17.9	21.1	19.7	19.1	20.8	12.6	20.6	20.8	16.6
3.6	6.9	4.5	6.9	6.0	5.2	7.3	5.0	6.0	5.9	5.2	7.1	4.4	6.0	6.9
0.06	0.10	0.09	0.12	0.10	0.09	0.11	0.09	0.09	0.10	0.09	0.13	0.07	0.10	0.10
7.0	13.6	8.9	13.6	10.7	8.8	12.7	8.5	10.3	10.4	9.5	14.2	8.2	10.7	12.7
14.6	10.6	15.4	14.7	14.1	14.4	12.4	13.9	13.1	13.5	14.2	12.8	14.2	11.6	12.0
1.99	1.60	1.72	1.14	1.59	1.80	1.55	1.96	1.72	1.59	1.82	1.12	1.81	1.81	1.27
0.21	0.16	0.14	0.07	0.11	0.16	0.11	0.19	0.18	0.33	0.10	0.63	0.18	0.29	0.10
0.03	0.05	0.02	0.02	0.03	0.04	0.03	0.05	0.05	0.03	0.03	0.03	0.04	0.04	0.04
1.4	2.1	1.7	1.9	0.9	1.4	1.6	2.8	2.2	1.9	0.4	2.5	2.0	3.8	5.5
99.2	99.9	99.1	99.7	99.3	100.1	99.2	99.8	99.6	99.7	100.1	99.1	99.1	99.1	99.3
77.6	77.8	78.0	77.7	76.0	75.2	75.7	75.2	75.5	75.9	76.3	78.1	76.8	76.1	76.7
24	18	40	86	–	38	23	388	25	403	49	1215	541	189	43
498	281	200	1234	–	765	892	–	1964	437	675	677	2665	–	4775
32	20	50	57	–	18	42	49	46	50	28	80	42	44	42
66	23	113	114	91	79	65	79	77	93	70	159	90	39	112
510	133	966	970	641	503	380	334	282	365	829	1149	480	145	642
54	108	73	131	78	59	79	67	69	79	154	192	66	70	59
17	15	15	13	15	16	15	16	16	15	16	12	16	15	16
23	59	39	46	43	47	51	47	41	44	36	56	35	51	27
33	29	32	26	34	36	28	32	34	30	30	36	35	29	36
27	54	29	53	–	35	49	–	53	–	43	–	–	–	35
0.19	0.33	0.12	0.16	–	0.17	0.26	–	0.26	–	0.13	–	–	–	0.13
7.3	2.7	4.4	0.9	–	2.5	1.8	–	4.1	–	2.1	–	–	–	3.2
46.7	38.7	37.0	22.8	–	36.6	32.2	–	38.4	–	28.0	–	–	–	36.1
0.16	0.18	0.12	0.08	–	0.19	0.12	–	0.33	–	0.15	–	–	–	0.38
0.03	0.05	0.03	0.02	–	0.04	0.03	–	0.08	–	0.05	–	–	–	0.09
0.48	0.40	0.23	0.18	–	0.38	0.30	–	0.67	–	0.91	–	–	–	0.82
0.03	0.02	0.02	0.02	–	0.02	0.02	–	0.29	–	0.09	–	–	–	0.05
1.18	1.25	0.98	0.65	–	1.07	0.86	–	0.99	–	1.13	–	–	–	1.44
647.3	494.2	551.0	398.5	–	581.7	546.1	–	603.0	–	461.3	–	–	–	473.7
0.37	0.41	0.51	0.52	–	0.44	0.34	–	0.44	–	0.49	–	–	–	0.67
5.6	3.0	7.5	9.8	–	6.7	5.6	–	6.2	–	7.4	–	–	–	8.9
2.59	2.51	2.19	1.90	–	2.53	2.19	–	2.50	–	2.14	–	–	–	3.18
5.69	5.17	5.38	5.22	–	5.87	5.04	–	5.68	–	5.16	–	–	–	7.65
0.82	0.68	0.82	0.86	–	0.85	0.72	–	0.82	–	0.79	–	–	–	1.12
3.71	2.81	4.12	4.48	–	4.11	3.28	–	3.80	–	3.73	–	–	–	5.15
0.94	0.59	1.21	1.49	–	1.11	0.92	–	1.02	–	1.02	–	–	–	1.44
0.60	0.49	0.63	0.63	–	0.64	0.60	–	0.61	–	0.58	–	–	–	0.68
1.09	0.58	1.36	1.64	–	1.24	1.00	–	1.15	–	1.28	–	–	–	1.63
0.16	0.09	0.22	0.28	–	0.19	0.16	–	0.19	–	0.21	–	–	–	0.26
0.96	0.51	1.35	1.75	–	1.18	1.01	–	1.11	–	1.24	–	–	–	1.58
0.19	0.11	0.27	0.35	–	0.23	0.19	–	0.22	–	0.27	–	–	–	0.32
0.53	0.28	0.74	0.91	–	0.66	0.52	–	0.58	–	0.71	–	–	–	0.87
0.41	0.28	0.59	0.77	–	0.49	0.44	–	0.48	–	0.61	–	–	–	0.72
0.06	0.04	0.08	0.11	–	0.08	0.06	–	0.07	–	0.09	–	–	–	0.10

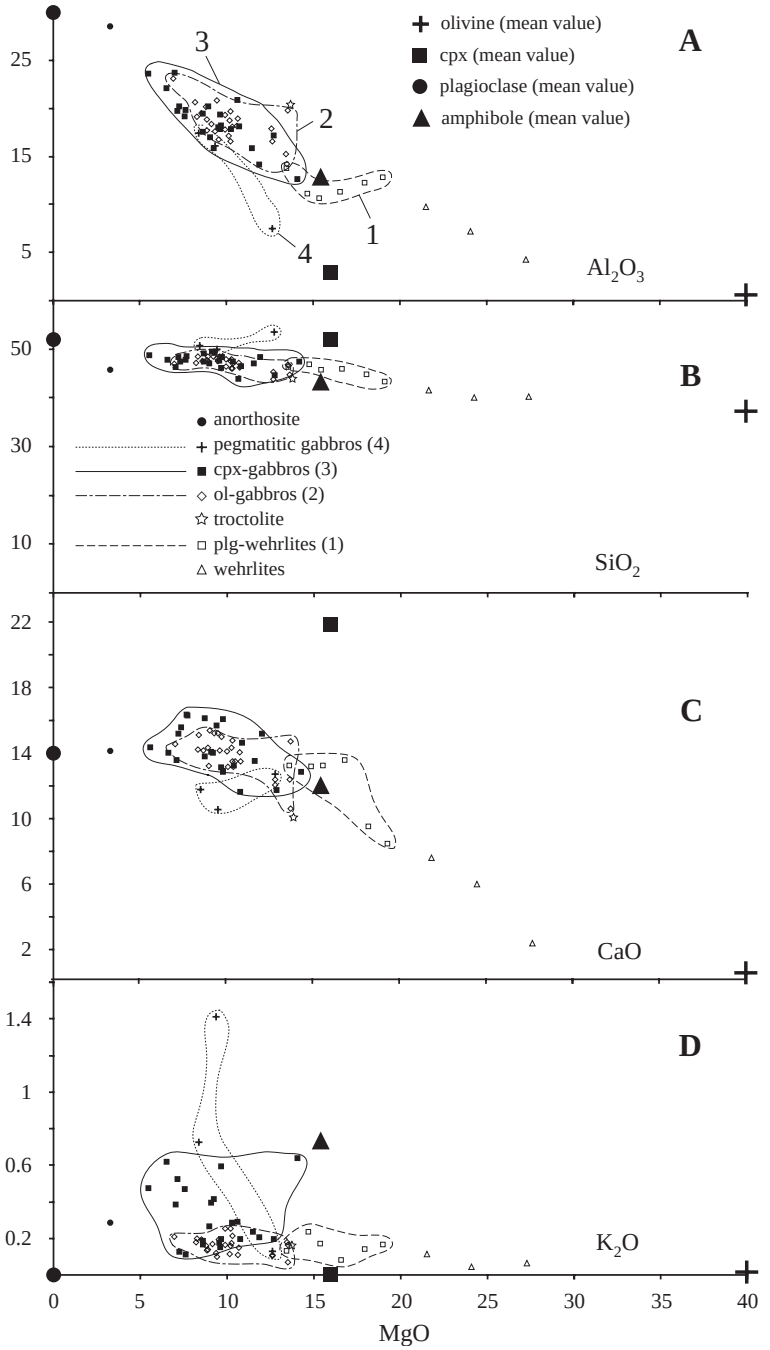

Fig. 5. Variation diagrams for major elements vs. MgO (in wt.%) for cumulative rocks of the Mont Collon. Average mineral compositional poles are given, showing that data point distributions are mainly defined by cumulus and intercumulus assemblages.

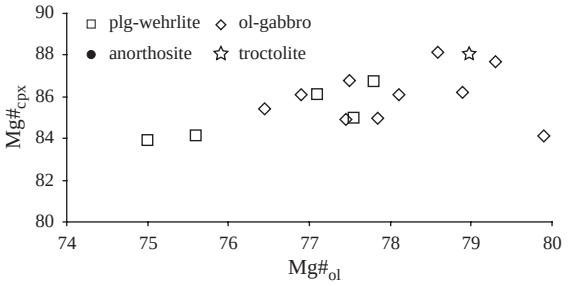

Fig. 6. Variation diagrams using $Mg\#_{cpx}$ vs. $Mg\#_{ol}$ of the Mont Collon cumulates.

Major elements plotted against MgO reveal two distinct groups of rocks (Fig. 5A–D): ultramafic cumulates, i.e. wehrlites and plagioclase-bearing wehrlites, with MgO contents ranging between 13 and 27 wt.% on the one hand and mafic cumulates, i.e. olivine- and clinopyroxene-bearing gabbros, with lower MgO contents (5–13 wt.%), on the other hand. Compositional fields of olivine and clinopyroxene gabbros generally overlap without significant chemical differences. The olivine- and clinopyroxene-gabbros display similar and large variations in Al_2O_3 (14.2–23.1 wt.%, 12.6–23.6 wt.%, respectively; Fig. 5A) and SiO_2 (43.8–47.6 wt.%, 43.8–49.4 wt.%, respectively; Fig. 5B). Clinopyroxene-gabbros are generally higher in K_2O (up to 0.63 wt.%; Fig. 5D) than all other rock types. Plagioclase-wehrlites have weak variations in Al_2O_3 (10.6–12.2 wt.%; Fig. 5A). P_2O_5 and TiO_2 do not show well-defined correlations with MgO (not shown). TiO_2 generally increases with decreasing MgO in plg-wehrlites, and scatter in the other cumulitic facies. MnO stays relatively constant (0.14–0.17 wt.%) in wehrlites and plagioclase-wehrlites, then tend to decrease from 0.14 wt.% to 0.06 wt.% in olivine- and clinopyroxene-bearing gabbros. The anorthosite displays the highest content in Al_2O_3 (28.5 wt.%; Fig. 5A) and Na_2O (2.30 wt.%) and the lowest one in TiO_2 (0.11 wt.%), FeO* (2.1 wt.%), MnO and P_2O_5 (0.02–0.03 wt.%), both close to the detection limits (0.01 wt.%). These compositional features are in good agreement with the mineralogy of anorthosite, dominated by plagioclase accumulation.

The whole-rock chemistry of pegmatitic gabbros does not largely differ from that of olivine- and clinopyroxene-gabbros (Fig. 5A–D). They display similar FeO* and Al_2O_3 contents, are enriched in TiO_2, Na_2O and K_2O and depleted in CaO (Fig. 5C), compared to the olivine and clinopyroxene gabbros. Off-trend values for Na, K and Ca might partly result from remobilization during greenschist facies recrystallization.

The whole-rock MgO content basically reflects the cumulus character of the various rocks (i.e. the modal abundances of cumulus olivine and/or clinopyroxene), and cannot be used as a differentiation

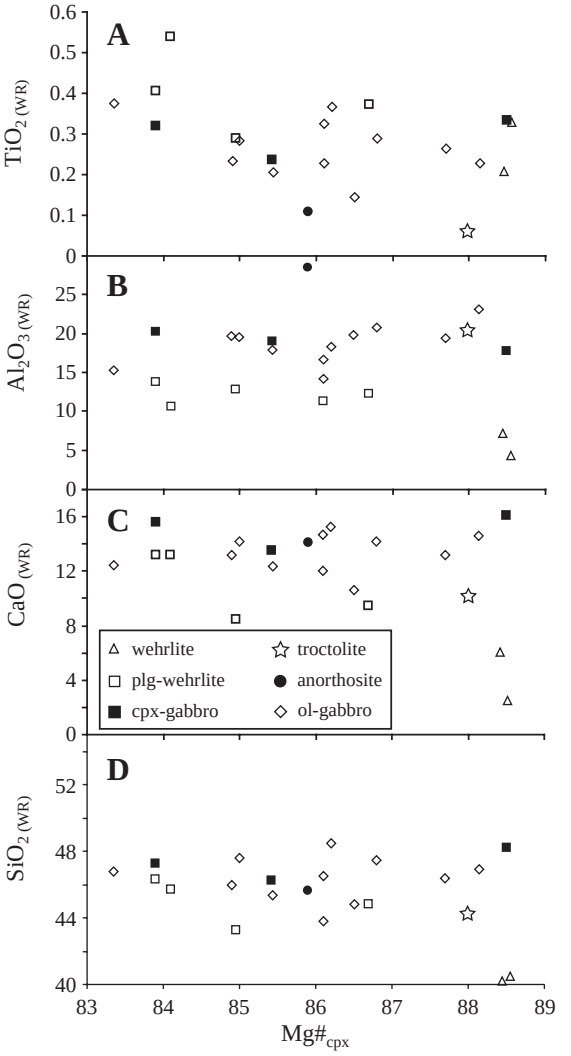

Fig. 7. Variation diagrams for selected major elements (in wt.%) vs. $Mg\#_{cpx}$ for cumulative rocks of the Mont Collon.

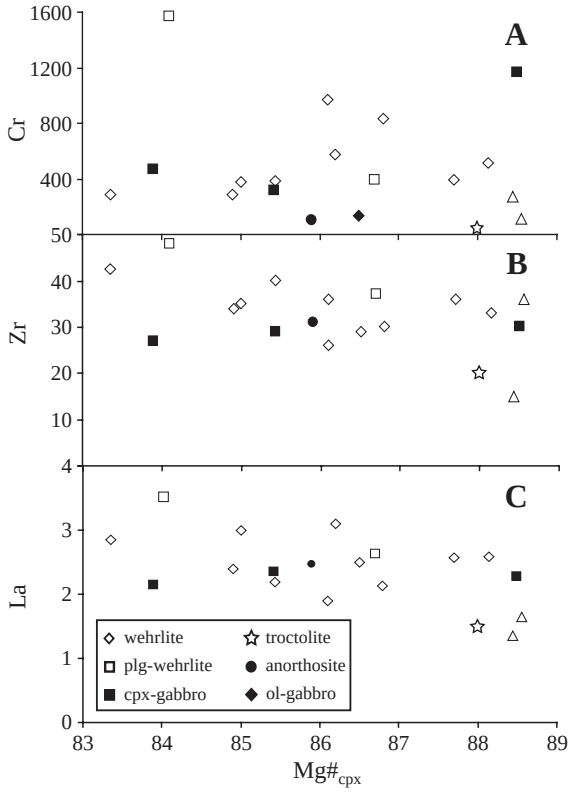

Fig. 8. Variation diagrams for selected trace elements (in ppm) vs. $Mg\#_{cpx}$ for cumulative rocks of the Mont Collon.

index in the interpretation of Fig. 5 diagrams. The same is true for Al_2O_3, CaO (Fig. 5A and C) and Na_2O, whose concentrations are strongly related to the plagioclase modal proportions in these rocks. This is well illustrated in Fig. 5A–C, where data points define linear (mixing) trends between mineral compositional poles.

As a proxy for the degree of differentiation of the Mont Collon cumulitic rocks, we will use the mg-number of clinopyroxene ($Mg\#_{cpx}$), which should reflect the degree of evolution of the melt from which it crystallized. $Mg\#_{cpx}$ shows a relatively good correlation with that of olivine ($Mg\#_{ol}$; Fig. 6), but has been preferred to the latter, as pyroxene is less prone to post-solidus re-equilibration than olivine and because it allows involvement of olivine-free rocks. $Mg\#_{cpx}$ lies within a very narrow range (83–89) over the whole set of lithologies, as does the whole-rock Mg# (73–80), which confirms that the Mont Collon cumulitic rocks record little magmatic differentiation at all. No significant (if any) trend can be observed when $Mg\#_{cpx}$ is plotted against major elements (e.g. TiO_2, Al_2O_3, CaO or SiO_2; Fig. 7A–D, with the possible exception of TiO_2, which tends to increase with increasing differentiation (i.e. decreasing $Mg\#_{cpx}$), as in classical tholeiitic differentiation. As expected, analytical points do not plot in the same way as in binary diagrams using MgO as index (Fig. 5). For example, some plagioclase-wehrlites and wehrlites, which are very high in MgO, plot on the differentiated side (i.e. lower $Mg\#_{cpx}$ than in other lithologies) of Fig. 7 diagrams.

7. Whole-rock trace-element chemistry

The trace-element behavior in the Mont Collon cumulitic rocks is quite variable (trace-element contents are given in Tables 6a and 6b). Compatible elements such as Ni, Co, Zn with K_D values >1 for early crystallizing minerals (olivine, clinopyroxene) usually show a good positive correlation when plotted against MgO (not shown). Others like Sr, Ba or Ga are negatively correlated with MgO, which reflects the dominant role of plagioclase in the cumulitic sequence when ferromagnesian minerals are less abundant. V, Cr and Y display a more complex, chevron-like evolution; with maximum concentrations at ca. 15 wt.% MgO, which is the limit between the gabbros (s.l.) and the wehrlites.

When trace elements are plotted against $Mg\#_{cpx}$ as a differentiation index, no clear correlation is observed (e.g. Cr; Fig. 8A), although some incompatible elements, such as Zr or REE, tend to increase with decreasing $Mg\#_{cpx}$ (Fig. 8). This absence of correlation is also illustrated in the well-preserved cumulitic sequence of the Dents de Bertol area (Fig. 9), where concentrations in incompatible trace elements like Zr, Y or Ba fluctuate largely and independently from the Mg# of the lithologies. Classical binary diagrams using Zr as differentiation index are mostly scattered (not shown), with few exceptions like for Nb, which is positively correlated with Zr (Fig. 10). The Zr vs. Nb diagram is particularly interesting; if the primitive troctolite MP240 plots as expected in the low concentration part of the diagram, the most enriched sample is plagioclase-wehrlite MP106, which is not the most

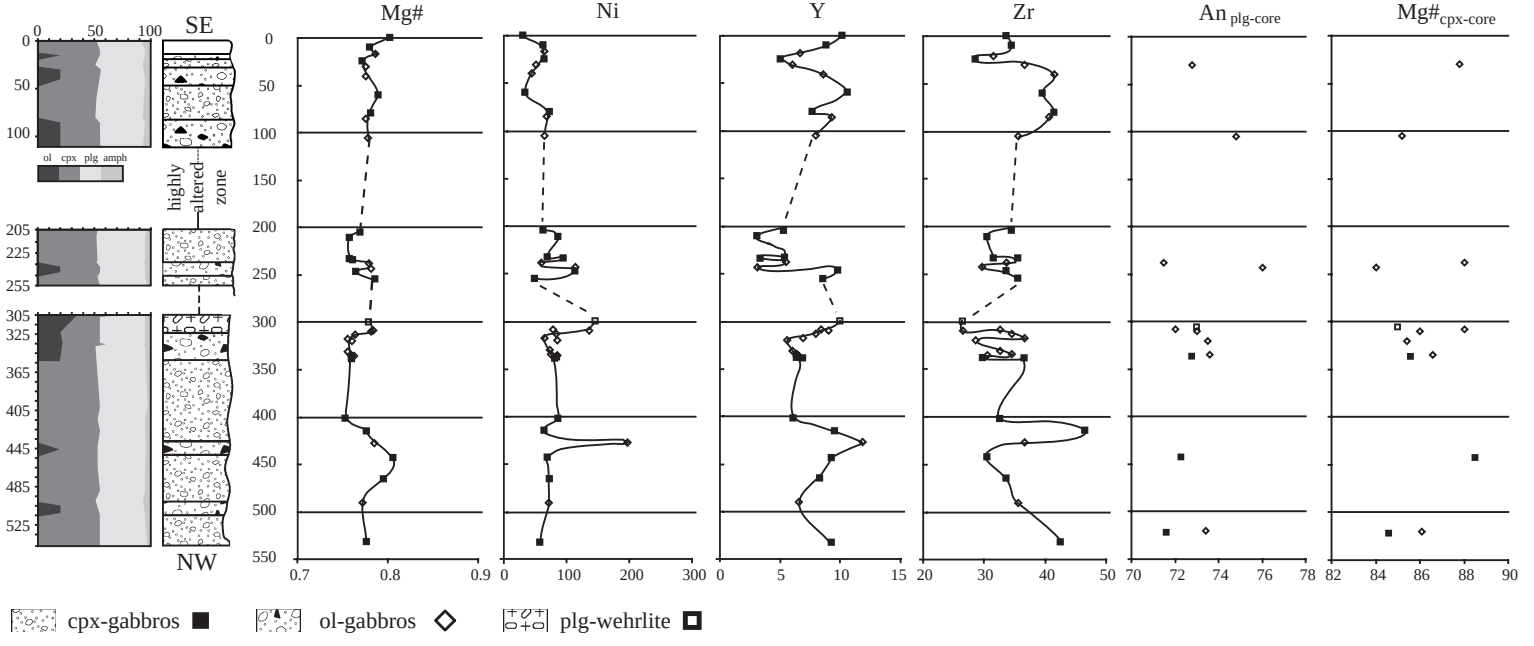

Fig. 9. Variation of modal proportions of minerals (vol.%), trace-element contents (ppm) and mineral compositions (An content in plagioclase and Mg# of clinopyroxene cores) along the Dents de Bertol cumulitic sequence. Mg#=molar ($Mg/(Fe_T+Mg)\times 100$. Vertical scale in meters.

Table 6b
Selected whole-rock major- and trace-element compositions (wehrlites, plg-wehrlites, troctolite, ol- and cpx-gabbros, pegmatitic gabbros and anorthosite)

Rock type	Cpx-gabbros																		Pgm gabbros		Troctolite	Anorthosite
Sampling area	DB	DB	DB	DB	DB	DB	DB	DB	DB	DB	DB	DB	DB	DB	DB	DB	DB	DB	MC	MC	DB	DB
Stratigraphic mark (m)	0	10	25	60	80	205	233	234	247	255	337	339	402	415	443	465	522	532	MP4	MP113	MP240	MP285
Sample number	MP120	MP122	M124	MP131	MP134	MP138	MP148	MP149	MP153	MP154	MP168	MP169	MP171	MP180	MP184	MP187	MP192	MP194				
SiO_2	49.3	46.9	44.6	49.1	46.9	47.7	48.6	46.1	46.3	48.5	46.3	46.0	47.3	49.4	48.2	47.8	47.3	48.3	50.6	53.4	44.2	45.7
TiO_2	0.37	0.35	0.23	0.41	0.34	0.23	0.22	0.15	0.35	0.33	0.24	0.26	0.23	0.37	0.33	0.31	0.32	0.37	0.53	1.17	0.06	0.11
Al_2O_3	15.8	15.8	17.1	17.5	20.2	22.0	23.6	23.6	14.0	19.8	18.9	19.3	17.8	16.9	17.8	19.1	20.2	19.7	17.4	7.5	20.2	28.5
FeO[a]	4.2	5.9	6.9	4.2	4.6	3.6	3.2	4.0	8.0	3.8	6.2	5.6	6.2	4.8	4.3	3.6	4.0	3.8	5.5	8.1	7.3	2.1
MnO	0.09	0.11	0.11	0.09	0.08	0.07	0.06	0.06	0.14	0.08	0.10	0.10	0.11	0.09	0.09	0.07	0.07	0.08	0.12	0.17	0.10	0.03
MgO	9.3	11.6	12.8	8.7	9.0	6.6	5.5	7.1	14.2	7.7	10.7	9.7	10.4	9.1	9.7	7.6	7.3	7.2	8.4	12.7	13.7	3.3
CaO	15.7	13.5	11.7	16.1	14.0	14.0	14.3	13.5	12.5	16.3	13.5	12.9	13.2	14.0	16.1	16.4	15.6	15.1	11.8	12.7	10.1	14.1
Na_2O	2.02	1.59	1.52	1.89	1.85	1.93	2.18	1.73	1.36	1.87	1.58	1.86	1.85	2.02	1.57	1.59	1.77	2.26	2.79	1.83	1.49	2.30
K_2O	0.41	0.23	0.19	0.19	0.26	0.61	0.47	0.38	0.45	0.11	0.15	0.59	0.28	0.39	0.15	0.47	0.13	0.52	0.73	0.13	0.16	0.28
P_2O_5	0.03	0.04	0.04	0.04	0.04	0.03	0.03	0.02	0.04	0.02	0.03	0.03	0.02	0.05	0.02	0.03	0.03	0.03	0.07	0.05	0.03	0.02
LOI	1.7	2.9	3.9	1.3	2.3	2.4	1.3	2.0	2.6	1.4	2.0	2.8	2.3	1.8	1.7	2.3	3.0	1.8	1.7	1.3	1.8	2.4
Total	99.0	99.1	99.1	99.6	99.7	99.2	99.5	98.8	100.1	100.0	99.8	99.1	99.7	99.1	100.0	9.4	99.7	99.3	99.7	99.1	99.1	98.8
Mg#	79.9	77.6	76.8	78.6	77.8	76.6	75.4	75.8	76.1	78.2	75.6	75.6	74.9	77.3	80.2	79.2	76.4	77.3	73.1	75.0	77.0	73.9
in ppm																						
Cu[a]	10	9	10	20	35	–	26	–	30	25	31	453	275	–	33	1758	45	–	18	n.d.	11	–
S[a]	27	9	11	1027	303	–	371	–	–	66	1830	–	–	–	5	577	1393	–	69	n.d.	247	–
Sc[a]	29	50	39	19	28	–	23	–	74	21	42	61	47	–	45	45	50	–	35	n.d.	14	–
V[b]	189	134	70	158	99	80	66	39	113	112	81	96	80	119	135	142	74	121	110	189	7	15
Cr[b]	1468	785	395	711	300	410	404	282	1011	900	310	372	272	626	1166	1670	467	912	233	886	36	102
Ni[b]	25	58	59	28	68	57	65	89	109	44	78	76	82	59	65	67	115	53	54	82	117	58

Ga[b]	13	14	14	15	16	15	17	16	13	16	15	15	15	13	15	15	14	16	16	12	15	19
Zn[b]	28	47	48	29	36	27	26	30	63	31	43	44	54	36	35	30	55	29	178	85	50	21
Zr[b]	33	34	28	39	41	34	35	31	33	35	29	36	32	46	30	33	27	42	52	62	20	31
Co	–	–	–	26	32	–	–	–	–	27	65	–	–	–	31	–	52	25	36	48	51	14
Cs	–	–	–	0.09	0.16	–	–	–	–	0.09	0.18	–	–	–	0.11	–	0.35	0.26	0.36	0.04	0.32	0.24
Rb	–	–	–	3.3	5.7	–	–	–	–	1.8	4.3	–	–	–	3.0	–	1.6	16.4	29.6	2.3	2.9	10.6
Ba	–	–	–	37.9	49.9	–	–	–	–	35.6	38.1	–	–	–	37.3	–	29.5	83.3	188.4	21.0	32.7	41.7
Th	–	–	–	0.24	0.38	–	–	–	–	0.12	0.11	–	–	–	0.21	–	0.12	0.23	0.90	3.35	0.07	0.10
U	–	–	–	0.09	0.08	–	–	–	–	0.03	0.03	–	–	–	0.05	–	0.02	0.07	0.70	1.48	0.02	0.02
Nb	–	–	–	0.52	1.33	–	–	–	–	0.31	0.53	–	–	–	0.24	–	0.31	0.47	3.56	11.24	0.05	0.27
Ta	–	–	–	0.03	0.08	–	–	–	–	0.02	0.52	–	–	–	0.02	–	0.02	0.05	0.23	0.72	0.00	0.02
Pb	–	–	–	1.04	2.10	–	–	–	–	2.10	0.96	–	–	–	1.05	–	1.18	1.29	38.18	1.57	0.68	1.13
Sr	–	–	–	451.8	520.7	–	–	–	–	550.2	573.9	–	–	–	433.6	–	445.1	610.8	503.9	121.1	563.6	737.2
Hf	–	–	–	1.32	0.61	–	–	–	–	0.52	0.39	–	–	–	0.58	–	0.37	0.60	0.67	2.29	0.08	0.14
Y	–	–	–	11.3	8.2	–	–	–	–	8.9	6.7	–	–	–	9.2	–	5.9	9.1	16.1	24.7	0.9	1.7
La	–	–	–	2.72	3.08	–	–	–	–	2.26	2.22	–	–	–	2.28	–	2.15	3.05	6.11	6.51	1.47	2.47
Ce	–	–	–	7.01	7.45	–	–	–	–	5.65	5.11	–	–	–	5.70	–	5.06	7.31	15.36	17.62	2.72	4.61
Pr	–	–	–	1.11	1.10	–	–	–	–	0.92	0.79	–	–	–	0.90	–	0.73	1.10	2.18	2.73	0.32	0.59
Nd	–	–	–	5.73	4.94	–	–	–	–	4.58	3.67	–	–	–	4.58	–	3.53	5.23	9.39	12.36	1.25	2.42
Sm	–	–	–	1.66	1.34	–	–	–	–	1.35	1.01	–	–	–	1.40	–	0.95	1.50	2.48	3.69	0.22	0.45
Eu	–	–	–	0.72	0.69	–	–	–	–	0.71	0.61	–	–	–	0.66	–	0.52	0.70	0.77	0.86	0.35	0.54
Gd	–	–	–	1.95	1.57	–	–	–	–	1.55	1.20	–	–	–	1.61	–	1.03	1.63	2.60	3.83	0.15	0.40
Tb	–	–	–	0.31	0.24	–	–	–	–	0.27	0.19	–	–	–	0.26	–	0.17	0.26	0.43	0.64	0.03	0.06
Dy	–	–	–	1.95	1.44	–	–	–	–	1.62	1.13	–	–	–	1.60	–	1.05	1.59	2.51	4.05	0.14	0.31
Ho	–	–	–	0.40	0.29	–	–	–	–	0.32	0.23	–	–	–	0.33	–	0.21	0.32	0.51	0.84	0.03	0.06
Er	–	–	–	1.07	0.79	–	–	–	–	0.87	0.61	–	–	–	0.92	–	0.57	0.84	1.41	2.31	0.07	0.16
Yb	–	–	–	0.92	0.64	–	–	–	–	0.69	0.50	–	–	–	0.71	–	0.48	0.70	1.14	2.05	0.08	0.12
Lu	–	–	–	0.13	0.09	–	–	–	–	0.10	0.07	–	–	–	0.10	–	0.07	0.11	0.17	0.29	0.01	0.02

Major-elements and some traces determined by X-ray fluorescence (XRF). (–): not determined. Other trace elements measured on a Fisons VG PlasmaQuad+ ICPMS.

[a] XRF trace-element analysis using classical short measurement time procedure (15 min).

[b] XRF analysis using long measurement time procedure (180 min).

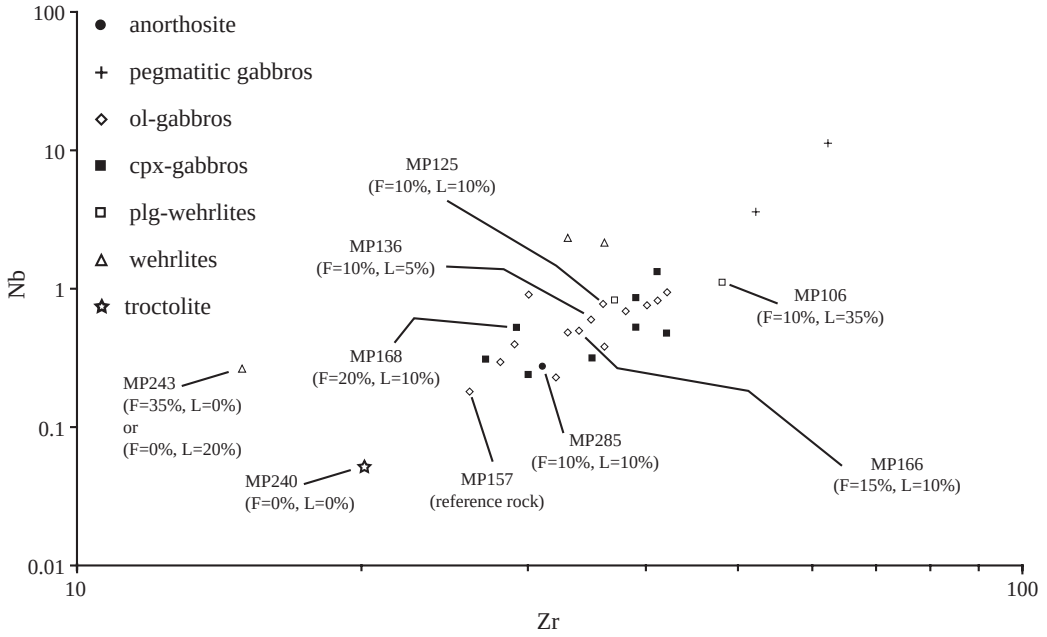

Fig. 10. Variation diagram of Nb (in ppm) using Zr as differentiation index. Sample labels (MPxxx) are reported with the corresponding modeled F and L values.

evolved rock-type of the massif. In other words, the incompatible trace-element content of the Mont Collon lithologies is not solely controlled by their cumulitic mineralogy, or by their degree of differentiation, but rather by the amount and composition of trapped interstitial liquid, as will be demonstrated later on by quantitative modeling.

8. Multi-element normalized diagrams

Wehrlites exhibit smooth REE patterns with low and variable contents ($\sum$REE ranges from 17.58 to 29.59 ppm), and a more or less marked negative Eu anomaly. Plagioclase-wehrlites show relatively flat patterns ($1.84 < La_N/Yb_N < 1.93$; $0.89 < La_N/Sm_N < 0.95$, and $Sm_N/Yb_N = 2$) with slightly higher concentrations (9 to 15 times the chondritic values). The troctolite is characterized by the lowest REE content ($\sum$REE = 6.85 times the chondritic abundances) and the strongest positive Eu anomaly (Eu/Eu* = 5.77). This rock is enriched in LREE ($La_N/Yb_N = 13.20$, $La_N/Sm_N = 4.27$) and displays a relative flat Medium to HREE pattern ($Sm_N/Yb_N = 3.08$). Ol- and cpx-gabbros display similar REE patterns, slightly enriched in LREE (La_N/Yb_N up to 3.67) and characterized by more or less marked positive Eu anomalies, showing the important role of plagioclase accumulation in the genesis of these rocks. Among the olivine gabbros, sample MP152 differs significantly from the others by a significant LREE enrichment ($La_N/Yb_N = 6.48$) and lower REE contents ($\sum$REE = 14.13 ppm), making it more similar to the troctolite than to olivine-gabbros. Plagioclase accumulation, which represents the most significant feature of the anorthositic layer, is reflected by its marked positive Eu anomaly (Eu/Eu* = 3.87), which nevertheless is lower than in the troctolite. Anorthosite differs from the gabbros by a REE pattern which is enriched in LREE [(La/Yb) = 14.24]. Pegmatitic gabbros exhibit REE patterns similar to those of the other gabbros, but with higher (and highest) REE contents (average $\sum$REE = 51.43 ppm), and a small Eu negative anomaly (Eu/Eu* close to 1).

The various Mont Collon lithologies have very similar multi-element primitive-mantle normalized diagrams. Typical features are negative anomalies in Nb–Ta, Zr–Hf, and Ti, and positive anomalies in Sr and Eu. All cumulitic rocks are more or less enriched in Th, U and LILE and depleted in HREE and Y. The pegmatitic gabbros differ from the

ultramafic (wehrlites) and mafic (gabbros s.l.) cumulates by the absence of the Nb, Ta, Zr, Hf and Ti negative anomalies, a significant enrichment in U, Th and a marked depletion in some LILE, except for Rb and Ba, which were probably remobilized by late-magmatic fluids (plagioclase is always heavily altered).

9. Trace-element mineral chemistry

9.1. Clinopyroxene

Chemical data are reported in Table 5. The REE contents (about 10 times the chondritic abundances) and patterns of clinopyroxenes are very similar whatever the rock type. They are depleted in La and Ce, and enriched in Nd and Sm. Gabbro clinopyroxenes exhibit a marked negative Eu anomaly, which is less important in clinopyroxenes of ultramafic cumulates. There is no correlation between REE content and the Eu anomaly. The main difference in the cpx REE patterns lies in the Nd and Sm enrichment, which appears to be more important in some gabbros (MP191, MP150, MP168). Clinopyroxenes from troctolites display REE patterns similar to those of the olivine-bearing gabbros. Multi-elements primitive-mantle normalized diagrams of clinopyroxene do not show differences related to the rock-type and are characterized, like those for whole-rocks, by (i) Nb, Ta, Zr, Hf negative anomalies, (ii) a depletion in LILE, HREE and Y, and (iii) an enrichment in Th. The only difference lies in the presence of Sr and Eu negative anomalies in the clinopyroxenes. These geochemical similarities between clinopyroxenes and whole-rock show that clinopyroxene is a major host for trace elements in the Mont Collon cumulates.

9.2. Plagioclase

HREE in plagioclases (from Ho to Lu) are always below detection limits. REE patterns of plagioclase are characterized by an important enrichment in La and Ce, relative to Nd and Sm, (La_N/Sm_N=27.6) and a higher (La_N/Dy_N) ratio. All analyzed plagioclases exhibit a large positive Eu anomaly. Multi-element primitive-mantle normalized diagrams exhibit, like in the clinopyroxenes and whole-rocks, the ubiquitous Nb–Ta negative anomalies. Interestingly, plagioclases from plagioclase-wehrlite are enriched in Rb (up to 10 times the primitive mantle) with respect to other rock types.

9.3. Amphibole

Amphiboles have higher REE contents than clinopyroxenes (about 30 times the chondrite, but their chondrite-normalized patterns are similar and do not depend on the rock type. On the other hand, multi-element primitive-mantle normalized diagrams are very different from those of clinopyroxenes, because they show positive Nb, Ta, Zr and Hf anomalies, as expected from the high distribution coefficients of amphiboles for these elements. Conversely, Sr is relatively depleted, as in clinopyroxenes, because this element has a higher affinity for plagioclase.

9.4. In-situ crystallization modeling

Although strongly layered, the Mont Collon intrusion does not present clear differentiation trends. As illustrated by the Dents de Bertol sequence (Fig. 9), major element contents of the main lithologies do not vary systematically and largely overlap, the Mg# is monotonous, modal abundance of major minerals remains roughly constant. In the same time, concentrations in incompatible-element like Zr, Nb, Y, Ba and REE vary considerably. As stated by Langmuir (1989), this feature is typical of in-situ crystallization, where gabbros form in a solidification zone with an unknown proportion of cumulates and interstitial liquid. In this situation, the major-element composition of a gabbro cumulate would be close to that of the magma from which it crystallizes and remain constant during differentiation, whereas incompatible trace-element contents would be controlled by the variable amount of interstitial liquid. In the Mont Collon cumulitic sequence, water-rich interstitial liquid is documented by intercumulus Ti-pargasite with high concentrations of incompatible-elements. Laser ablation ICP-MS microanalysis shows that there is no trace element zoning in minerals (but contents might vary from one crystal to the other within a sample), which means that they locally re-

equilibrated with the interstitial liquid at subsolidus conditions (Hermann et al., 2001). In other words, the trace-element composition of mineral phases directly records the presence and the proportion of a former interstitial liquid.

To quantify this process, we thereafter use the model of in-situ crystallization developed by Hermann et al. (2001). The idea is to calculate REE patterns of all mineral phases in a given sample starting from a primitive gabbro liquid and using the equation of Langmuir (1989). These calculated patterns are then fitted to actual LA-ICP-MS data in adjusting F (degree of differentiation) and L (proportion of interstitial liquid) in Eq. (4). For each set of mineral data, a best fit can be calculated with corresponding F and L values.

10. Parameters and procedure

10.1. Partition coefficients

The first step is to determine REE partition coefficients between minerals and melt, starting with those for clinopyroxene ($D_{cpx/Melt}$). Unfortunately, available data sets in the literature are either incomplete or are not applicable to our clinopyroxene compositions, which are high in CaO (up to 23 wt.%) and low in Al_2O_3 (<4 wt.%). We therefore used the predictive model of Wood and Blundy (1997) with analysis MP157cpx3-2, selected for its lowest REE content ($\sum$REE=25.08 ppm), high Mg# (87.8), weak Eu negative anomaly (Eu/Eu*~0.95) and the low Nb–Zr content of the host rock. Calculations were done using a K_{Fe-Mg}^{ol} of 0.30, and the pressure and temperature calculated in the above P/T section. $D_{pl/M}$, $D_{ol/M}$ and $D_{amph/M}$ (for plagioclase, olivine and amphibole) are then calculated using mineral/cpx partition coefficients, according to Eqs. (1a)–(1c) (the REE content of each mineral is measured by LA-ICP-MS):

$$REE_{pl}/REF_{cpx} = D_{pl/M} = \text{cste} \Rightarrow D_{pl/M} = D_{cpx/M} * REE_{pl}/REE_{cpx} \quad (1a)$$

$$REE_{amph}/REE_{cpx} = D_{amph/M}/D_{cpx/M} = \text{cste} \Rightarrow D_{amph/M} \quad (1b)$$

$$REE_{ol}/REE_{cpx} = D_{ol/M}/D_{cpx/M} = \text{cste} \Rightarrow D_{ol/M} \quad (1c)$$

The bulk rock partition coefficient $D_{rock/M}$ is calculated (Eq. (2a)) assuming the modal content of MP157 olivine-gabbro (48% cpx, 35% plagioclase, 15% olivine and 2% pargasite). To calculate the enrichment of elements in the residual melt, we introduce the $D'_{rock/M}$parameter (Eq. (2b)) in the "Rayleigh fractionation" part of the in-situ crystallization equation, which takes into account that an average of 10% of melt is trapped during differentiation (this parameter does not affect drastically the modeled REE contents).

$$D_{rock/M} = 0.40D_{cpx/M} + 0.20D_{pl/M} + 0.35D_{ol/M} + 0.05D_{amph/M} \quad (2a)$$

$$D'_{rock/M} = 0.90D_{rock/M} + 0.10 \quad (2b)$$

Fig. 11. Upper left: REE partition coefficient values between mineral and melt ($D_{mineral/Melt}$), respectively whole-rock and melt ($D_{rock/Melt}$). For clinopyroxene, $D_{cpx/M}$ are calculated according to the predictive model of Wood and Blundy (1997). Partition coefficients for plagioclase/melt and amphibole/melt are calculated from $D_{cpx/melt}$ and LA-ICPMS data (see text). $D_{rock/M}$=bulk partition coefficient without trapped liquid, $D'_{rock/M}$=bulk partition coefficient with 10% interstitial liquid remaining in the cumulitic mineral assemblage (see text). Upper right: Chondrite-normalized REE pattern of the reference clinopyroxene (MP157cpx3-2) used for in-situ crystallization modeling. Other diagrams: comparison of measured (open symbol) and calculated (filled symbol) chondrite-normalized REE patterns of clinopyroxene (■), plagioclase (●) and amphibole (□). F=degree of differentiation with respect to the reference clinopyroxene and L=amount of trapped liquid. Normalization to the chondrite after Sun and Mc Donough (1989).

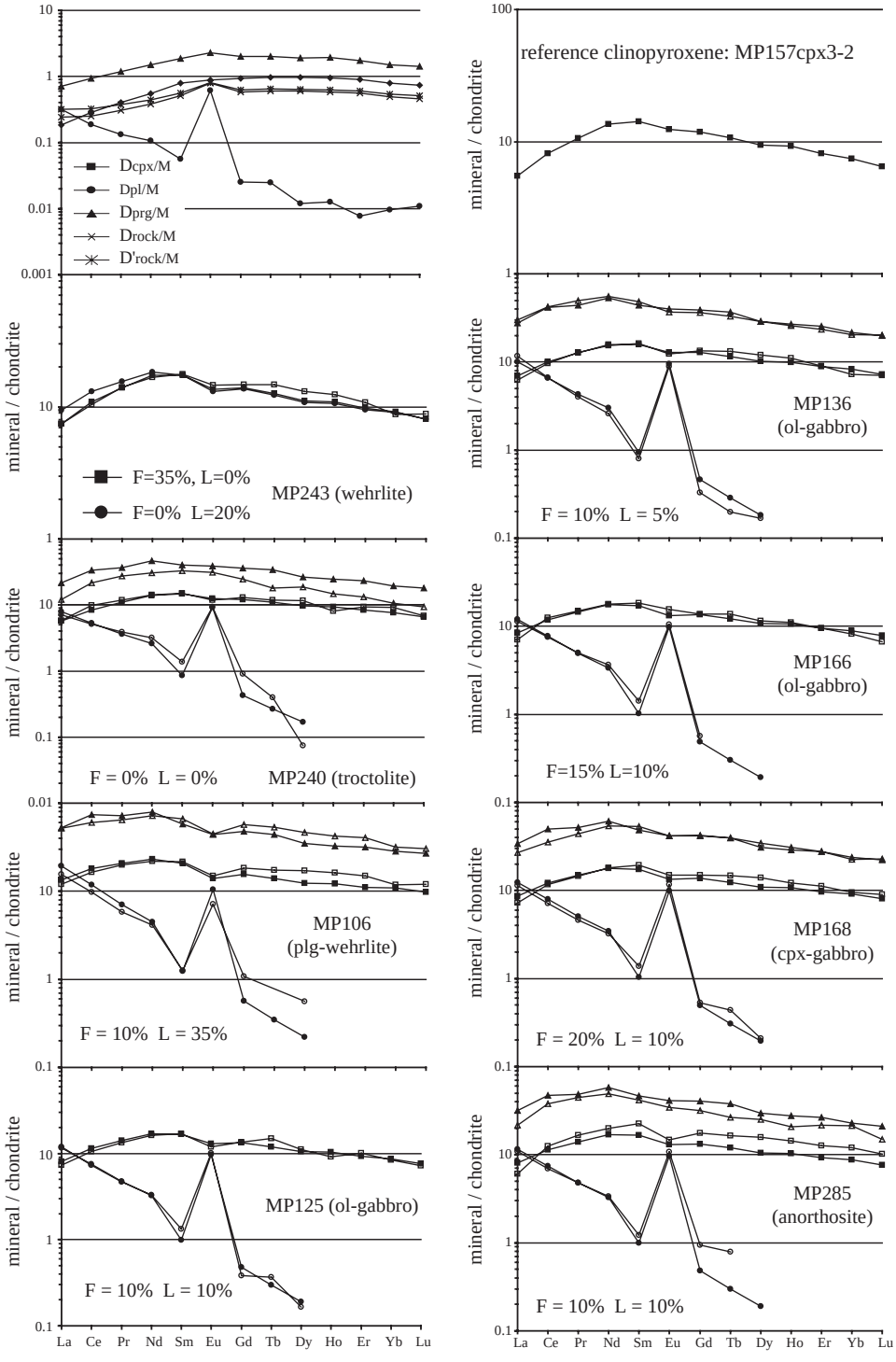
Dcpx/M
Dpl/M
Dprg/M
Drock/M
D'rock/M
mineral / chondrite
reference clinopyroxene: MP157cpx3-2
F=35%, L=0%
F=0% L=20%
MP243 (wehrlite)
MP136
(ol-gabbro)
F = 10% L = 5%
F = 0% L = 0%
MP240 (troctolite)
MP166
(ol-gabbro)
F=15% L=10%
MP106
(plg-wehrlite)
F = 10% L = 35%
MP168
(cpx-gabbro)
F = 20% L = 10%
MP125 (ol-gabbro)
F = 10% L = 10%
MP285
(anorthosite)
F = 10% L = 10%
La Ce Pr Nd Sm Eu Gd Tb Dy Ho Er Yb Lu

10.2. Calculation of the initial magma composition

The starting liquid L_o is obtained using the REE composition of the "reference" clinopyroxene (i.e. with lowest REE content, MP157cpx3-2, Fig. 11):

$$L_o = \mathrm{REE}_{cpx}/D_{cpx/M} \tag{3}$$

10.3. Estimation of the degree of differentiation (F) and proportion of intercumulus liquid (L)

The whole-rock REE content (REE_{rock}) can be expressed as the sum of cumulus phases and interstitial liquid, given by Langmuir equation (Eq. (4)), or as the sum of the different mineral contributions (Eq. (5)). Boundary limits for Eq. (4) are set by $L=0$ (pure cumulate) and $L=100\%$ (frozen liquid).

$$\mathrm{REE}_{rock} = \text{cumulus phase} + \text{interstitial melt}$$

$$= L_o(1-F)^{D'_{rock/M-1}}\left[D_{rock/M}(1-L)+L\right] \tag{4}$$

$$= 0.48\mathrm{REE}_{cpx} + 0.35\mathrm{REE}_{pl} + 0.15\mathrm{REE}_{ol} + 0.02\mathrm{REE}_{amph} \tag{5}$$

Combining Eqs. (4) and (5) with Eqs. (1a)–(1c) (i.e. $\mathrm{REE}_{pl}=\mathrm{REE}_{cpx}*(D_{pl/M}/D_{cpx/M})$, etc.), we extract the calculated REE content of clinopyroxene (REEc_{cpx}, Eq. (6a)) and subsequently that of other mineral species (Eqs. (6b) and (6c)).

$$\Rightarrow \mathrm{REEc}_{cpx} = \frac{\left[L_o(1-F)^{D'_{rock/M-1}} \times \left[D_{rock/M}(1-L)+L\right]\right]}{\left[0.48 + 0.35\left(D_{pl/M}/D_{cpx/M}\right) + 0.15\left(D_{ol/M}/D_{cpx/M}\right) + 0.02\left(D_{amph/M}/D_{cpx/M}\right)\right.} \tag{6a}$$

$$\Rightarrow \mathrm{REEc}_{pl} = \mathrm{REEc}_{cpx} \times \left(D_{pl/M}/D_{cpx/M}\right) \tag{6b}$$

$$\Rightarrow \mathrm{REEc}_{amph} = \mathrm{REEc}_{cpx} \times \left(D_{amph/M}/D_{cpx/M}\right) \tag{6c}$$

The calculated $\mathrm{REEc}_{mineral}$ are then compared with and fitted to the real LA-ICP-MS mineral data of the tested sample in adjusting F and L by a trial and error procedure (Fig. 11).

11. Discussion: results and limitation of the model

Examples of measured vs. modeled mineral compositions are given in Fig. 11 for a wehrlite (MP243), a plg-wehrlite (MP106), ol-gabbros (MP125, MP136 and MP166), a cpx-gabbro (MP168), the troctolite (MP240) and the anorthosite (MP285). Measured compositions are means of several LA-ICP-MS analyses for all mineral species. Because of the structure of Eq. (4), L and F do not influence the calculated mineral REE contents in the same way. For instance, L has a much stronger effect on the LREE contents of low $D_{min/melt}$ minerals such as clinopyroxene than F. Thus, clinopyroxenes with highest amounts of Sm or Nd are modeled with the highest L values. More generally, the higher the REE contents of minerals, the higher is the proportion of calculated trapped liquid L. As a consequence of the differentiated effect of F and L in Eq. (4), we found in most cases unique sets of F and L values to fit accurately

the measured mineral compositions. A notable exception is wehrlite MP243, for which REE clinopyroxene contents can be modeled with $F=0\%$ and $L=20\%$ or better with $F=35\%$ and $L=0\%$ (Fig. 11). This duality is certainly related to the absence of plagioclase and amphibole in the sample, which usually provide additional constraints to the fitting procedure. The main difference between the two calculations resides in a higher LREE content for $F=0\%/L=20\%$ than for $F=35\%/L=0\%$, which further illustrates that F is less sensitive than L to (Light)REE concentrations.

Apart from plg-wehrlite MP243, the calculated degree of fractionation F is comprised within a narrow range of 0 to 20% for all tested samples. Anorthosite MP285 displays an F value of 10%, suggesting that segregation of anorthositic material might occur early in the magma chamber. This result is in agreement with field and petrological data, but deserves confirmation, as the measured REE contents of the rare crystals of amphibole and clinopyroxene found in anorthosite MP285 cannot be fitted simultaneously (Fig. 11). The REE content of the modeled amphibole is too high, while that of the clinopyroxene is too low with a given set of F and L values. MP285 anorthosite mainly consists of plagioclase (95 vol.%), which means that the measured clinopyroxenes and amphiboles might not be statistically representative.

There is no clear correlation between the calculated degree of differentiation F and the differentiation index of the tested samples expressed by their $Mg\#_{cpx}$ (Fig. 12). Nevertheless, F values of 0% plot preferentially on the high $Mg\#_{cpx}$ side of the diagram, as expected for weakly differentiated rocks. Additional data would be necessary to confirm this trend, but in any case, F values between 0 and 20% are geologically reasonable within the observed range of $Mg\#_{cpx}$.

The calculated proportion of trapped liquid L is more variable than F. Some samples are modeled as pure cumulates, without interstitial liquid ($L=0\%$, i.e. troctolite MP240), whereas the maximum L is 35% (plg-wehrlite MP106). These values are consistent with mineralogical and chemical features. There is a good correlation between L values and the modal proportions of magmatic amphibole (Fig. 13A), which makes this mineral a good proxy for the proportion of interstitial melt. L is also consistent with whole-rock concentrations of incompatible trace elements such as

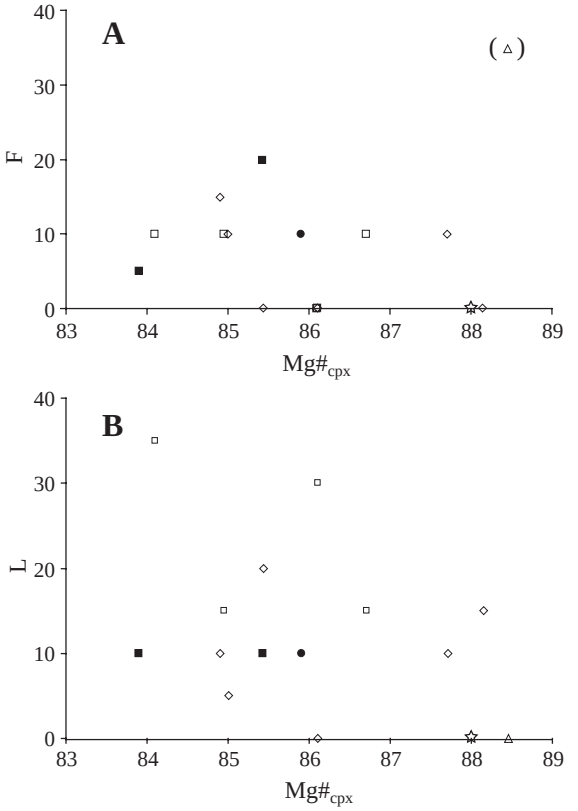

Fig. 12. Variation diagrams for a series of modeled samples between the $Mg\#_{cpx}$ and (A) the degree of differentiation F and (B) the calculated percentage of interstitial liquid L.

Zr (Fig. 13B), unlike F (Fig. 13C). This confirms our assumption that incompatible trace-element distribution is essentially controlled by the proportion of interstitial liquid L rather than by the degree of differentiation F.

The proportion of trapped liquid L is not correlated with the $Mg\#_{cpx}$ of the tested samples (Fig. 12B), which is not surprising, as the proportion of interstitial melt in a cumulitic sequence is decoupled from the degree of evolution of the latter in a given range of magma composition. It must be pointed out that a large L might shift down $Mg\#_{cpx}$ by a few hundredth of unit through reequilibration between interstitial melt and cumulus clinopyroxene (Barnes, 1986). Interestingly, plagioclase core composition is somehow correlated with L values. Samples with lowest L contain the most anorthositic plagioclase (MP136 ($L=5\%$): plg_{core} An=82.6; MP125 ($L=10\%$): plg_{core} An=72.8; MP168 ($L=10\%$): plg_{core} An=72.8),

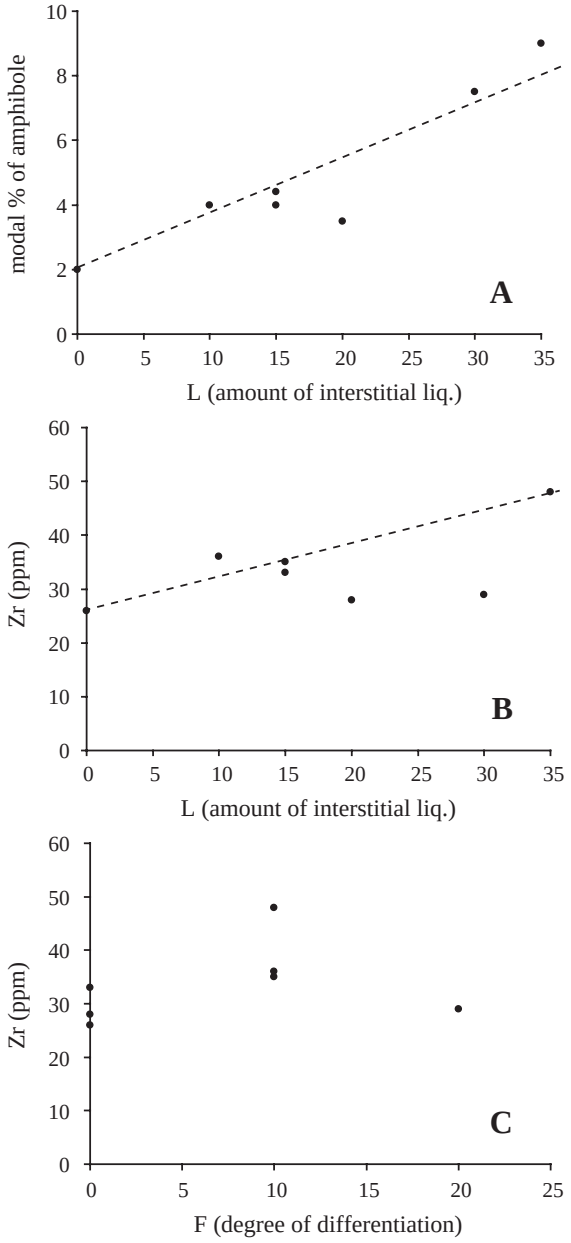

Fig. 13. Variation diagrams for a series of modeled samples between the calculated percentages of interstitial liquid (L) and (A) the modal proportion of interstitial amphibole, and (B the whole-rock Zr content. (C) The poor correlation between the calculated degree of differentiation (F) and the whole-rock Zr content of the modeled rocks.

whereas plagioclase in plg-wehrlite MP106 (L=35%) is significantly more sodic (plg_{core} An=63.1–69.2). This feature agrees well with the late intercumulus (thus more sodic) nature of plagioclase in plg-wehrlites.

The in-situ crystallization model reaches its limitations with rock containing high modal content of REE-bearing minerals (i.e. apatite or zircon), which strongly influence the REE budget. Mineral alteration and high modal proportion of zircon in pegmatitic gabbros prevents any quantitative modeling. But we suspect that these rocks represent almost pure, fluid-rich melts, differentiated, although without much plagioclase subtraction.

In this model, all non-cumulitic material has been considered as local interstitial melt L, trapped in the solidification zone. But field observation of veinlets of anorthositic composition locally crosscutting the layered lithologies evidence that some melt must have migrated through the cumulitic sequence and eventually been trapped in a more or less distant place. Such situations are open systems with mixing of intercumulus liquids of different origins and possibly contrasting compositions. The proposed model is not able to resolve these complex open systems, which are not well enough constrained, but migrating liquids could be partly responsible for the observed dispersion of points in some correlation diagrams like L vs. Zr (Fig. 13B).

Absence of significant differentiation in the cumulitic pile of Dents de Bertol, which is several hundred meters high, raises the question of how this sequence built up. Recurrent lithologies with similar cumulus mineral compositions point to an efficiently convective magma chamber, with possible periodic replenishment. Heterogeneities within initial Sr isotopic ratios (Monjoie et al., in preparation) strongly support the latter mechanism.

12. Conclusion

The Mont Collon intrusion is a weakly differentiated pluton despite its layered structure, as evidenced by its monotonous cumulus mineral compositions. Anorthosites are extremely rare and evolved facies like diorites have never been found. Uncoupling between monotonous major-element chemistry and highly variable incompatible trace-element concentrations are successfully modeled by an in-situ crystallization process. Quantitative modeling points

to 0 to 35% of interstitial liquid L in the cumulates for a maximum degree of differentiation F of 20% relative to the most primitive rock of the intrusion. L and F are quite variable along the cumulitic sequence, pointing to irregular compaction and convection (?) efficiency in the magma chamber as well as periodic replenishment. L is well correlated to the modal proportion of amphibole in the rock, which appear to be a good proxy for the proportion of intercumulus liquid at time of solidification. The model is not able to decipher between closed- and open-system for intercumulus liquid, but offers a good tool to establish the relative role of magma differentiation and mineral accumulation in mafic layered sequences.

Acknowledgements

We would like to thank G. Piccardo for thorough and helpful discussions, as well as A. Demant and P. Tricart for their suggestions. Reviews by J. Hermann and R. Latypov substantially improved this paper and are gratefully acknowledged. This study was financially supported by the Swiss National Science Foundation (project no. 20-050531.97).

Appendix A. Analytical procedures

Major- and some trace elements (Tables 6a and 6b) were analyzed by XRF at the Centre d'Analyse Minérale (University of Lausanne, Switzerland) using fused and pressed pellets, respectively. Accuracy on major elements is close to and less than 10% for trace elements. Whole-rock incompatible trace elements for whole-rocks have been determined by inductively coupled plasma spectrometry (ICP-MS VG-PQ^{2+}) at the Laboratoire de Géodynamique des Chaînes Alpines of the University J. Fourier (Grenoble, France), after acid dissolution, using procedures of Barrat et al. (1996). The accuracy on trace element concentrations is better than 3% for all the REE based on various standards and sample duplicates. Mineral compositions are given in Tables 1–5. Major- and minor elements in minerals were analyzed with a Cameca Camebax SX50 microprobe using a 15 kV acceleration voltage and different regulated beam currents, according to the mineral type (10 nA for plagioclase, 15 nA for amphiboles and 20 nA for olivine, pyroxenes and oxides). The calibration was made on specific natural mineral standards for each type of minerals. Trace-element measurements on minerals were made by laser-ablation ICP-MS using a 193 nm Ar–F Lambda Physics Excimer laser coupled with a Perkin-Elmer6100DRC ICPMS. NIST610 and 612 glasses were used as external standards, Ca and Si as internal standards after microprobe measurements on the pit sites. Ablation pit size varied from 40 to 60 μm. BCR2 basaltic glass was regularly used as a monitor to check for reproducibility and accuracy of the system. Results were always within ± 10% of the certified values.

References

Barnes S.J., 1986. The effect of trapped liquid crystallization on cumulus mineral compositions in layered intrusions. Contrib. Mineral. Petrol. 93, 524–531.

Barrat J.A., Keller F., Amosse J., Taylor R.N., Nesbitt R.W., Hirata T., 1996. Determination of rare earth elements in sixteen silicate reference samples by ICP-MS after Tm addition and ion exchange separation. Geostand. Newsl. 20 (1), 133–139.

Bigi, G., Castellarin, A., Coli, M., Dal Piaz, G.V., Sartori, R., Scandone, P., Vai, G.B., 1990. Structural model of Italy 1:500 000, sheet 1, C.N.R., Progetto Geodinamica, SELCA, Firenze.

Bonin B., Brändlein P., Bussy F., Desmons J., Eggenberger U., Finger F., Graf K., Marro Ch., Mercolli R., Oberhänsli R., Ploquin A., von Quadt A., von Raumer J.F., Schaltegger U., Steyrer H.P., Visonà D., Vivier G., 1993. Late Variscan magmatic evolution of the Alpine basement. In: von Raumer, J.F., Neubauer, F. (Eds.), Pre-Mesozoic Geology in the Alps. Springer-Verlag, pp. 171–202.

Bucher, K., Dal Piaz, G.V., Oberhansli, R, Gouffon, Y., Martinotti, G., Polino, R., 2003. Blatt 1347 Matterhorn. Geol. Atlas Schweiz, 1/25 000, Karte 107.

Bucher, K., Dal Piaz, G.V., Oberhansli, R, Gouffon, Y., Martinotti, G., Polino, R., 2004. Blatt 1347 Matterhorn. Geol. Atlas Schweiz, 1/25 000, Erlut. 107.

Bussy F., Venturini G., Hunziker J.C., Martinotti G., 1998. U–Pb ages of magmatic rocks of the western Austroapline Dent Blanche-Sesia Unit. Schweiz. Mineral. Petrogr. Mitt. 78, 163–168.

Bussy F., Hernandez J., Von Raumer J., 2000. Bimodal magmatism as a consequence of the post-collisional readjustment of the thickened Variscan continental lithosphere (Aiguilles Rouges-Mont Blanc massifs, western Alps). Trans. R. Soc. Edinb. 91, 221–233.

Dal Piaz G.V., 1993. Evolution of austro-alpine and upper penninic basement in the northwestern alps from variscan convergence to post-variscan extension. In: von Raumer, J.F., Neubauer, F.

(Eds.), Pre-Mesozoic geology in the Alps. Springer-Verlag, Berlin Heidelberg, pp. 327–344.

Dal Piaz G.V., 1999. The Austroalpine-Piedmont nappe stack and the puzzle of Alpine Tethys. Mem. Sci. Geol. 51 (1), 155–176.

Dal Piaz G.V., De Vecchi G., Hunziker J.C., 1977. The Austroalpine layered gabbros of the Matterhorn and Mt. Collon-Dents de Bertol. Schweiz. Mineral. Petrogr. Mitt. 57, 59–88.

Debon F., Cocherie A., Ménot R.-P., Vivier G., Barféty J.-C., 1994. Datation du plutonisme magnésien varisque des massifs cristallins externes des Alpes: l'exemple du Granite des Sept Laux (Massif de Belledonne, France). C.R.A.S. t. 318 (série II), 1497–1504.

Deer W.A., Howie R.A., Zussmann J., 1992. In: Longman (Ed.), An Introduction to the Rock-Forming Minerals, vol. 1. 696 pp.

Green D.H., Ringwood A.E., 1967. The genesis of basaltic magmas. Contrib. Mineral. Petrol. 15 (2), 103–190.

Hansmann W., Müntener O., Hermann J., 2001. U–Pb zircon geochronology of a tholeiitic intrusion and associated migmatites at a continental crust–mantle transition, Val Malenco, Italy. Schweiz. Mineral. Petrogr. Mitt. 81 (2), 239–255.

Hermann J., Rubatto D., 2003. Relating zircon and monazite domains to garnet growth zones: age and duration of granulite facies metamorphism in the Val Malenco lower crust. J. Metamorph. Geol. 21 (9), 833–852.

Hermann J., Müntener O., Günther D., 2001. Differentiation of mafic magma in a continental crust-to-mantle transition zone. J. Petrol. 42 (1), 189–206.

Holland T.J.B., Blundy J.D., 1994. Non-ideal interactions in calcic amphiboles and their bearing on amphibole–plagioclase thermometry. Contrib. Mineral. Petrol. 116, 433–447.

Holloway J.R., Burnham C.W., 1972. Melting relations of basalt with equilibrium water pressure less than total pressure. J. Petrol. 13, 1–29.

Irvine T.N., Baragar W.R.A., 1971. A guide to the chemical classification of the common volcanic rocks. Can. J. Earth Sci. 8 (5), 523–548.

Leake B.E., Woolley A.R., Arps C.E.S., Birch W.D., Gilbert M.C., Grice J.D., Hawthorne F.C., Kato A., Kisch H.J., Krivovichev V.G., Linthout K., Laird J., Mandarino J.A., Maresch W.V., Nickel E.H., Rock N.M.S., Schumacher J.C., Smith D.C., Stephenson N.C.N., Ungaretti L., Whittaker E.J.W., Guo Y., 1997. Nomenclature of amphiboles; report of the subcommittee on amphiboles of the International Mineralogical Association, Commission on New Minerals and Mineral Names. Can. Mineral. 35 (1), 219–246.

Langmuir C.H., 1989. Geochemical consequences of in-situ crystallization. Nature 340, 199–205.

Loucks R.R., 1996. A precise olivine–augite Mg–Fe exchange geothermometer. Contrib. Mineral. Petrol. 125, 140–150.

Martinotti G., Hunziker J.C., 1984. The Austroalpine system in the Western Alps: a review. Mem. Soc. Geol. Ital. 29, 233–250.

Monjoie, P., Bussy, F., Lapierre, H., Schaltegger, U., Pfeifer, H.-R., Mulch, A. Precise, submitted for publication U/Pb and $^{40}Ar/^{39}Ar$ dating of the layered Permian Mafic Complex of the Mont Collon (Western Alps, Wallis, Switzerland). Schweiz. Mineral. Petrogr. Mitt.

Mulch A., Rosenau M., Doerr W., Handy M.R., 2002. The age and structure of dikes along the tectonic contact of the Ivrea–Verbano and Strona–Ceneri zones (Southern Alps, northern Italy, Switzerland). Schweiz. Mineral. Petrogr. Mitt. 82 (1), 55–76.

Nimis P., Ulmer P., 1998. Clinopyroxene geobarometry for magmatic rocks: Part 1. An extend structural geobarometer for anhydrous and hydrous, basic and ultrabasic systems. Contrib. Mineral. Petrol. 133, 122–135.

Rivalenti G., Garuti G., Rossi A., Siena F., Sinigoi S., 1980. Existence of different peridotite types and of a layered igneous complex in the Ivrea Zone of the Western Alps. J. Petrol. 22 (1), 127–153.

Sinigoi S., et al., 1994. Chemical evolution of a large mafic intrusion in the lower crust, Ivrea–Verbano Zone, northern Italy. J. Geophys. Res. 99 (B11), 21575–21590.

Springer W., Seck H.A., 1997. Partial fusion of basic granulites at 5 to 15 kbar: implications for the origin of TTG magmas. Contrib. Mineral. Petrol. 127, 30–45.

Sun S.S., Mc Donough W.F., 1989. Chemical and isotopic systematics of oceanic basalts: implications for mantle composition and processes. Spec. Publ.-Geol. Soc. Lond. 42, 313–345.

Thompson R.N., 1984. Dispatches from the basalt front: 1. Experiments. Proc. Geol. Assoc. 95, 249–262.

Tribuzio R., Thirlwall M.F., Messiga B., 1999. Petrology, mineral and isotope geochemistry of the Sondalo gabbroic complex (Central Alps, Northern Italy): implications for the origin of post-Variscan magmatism. Contrib. Mineral. Petrol. 136, 48–62.

Venturini G., Hunziker J.C., Pfeifer H.-R., 1996. Geochemistry of mafic rocks in the Sesia zone (Western Alps): new data and interpretations. Eclogae Geol. Helv. 89, 369–388.

von Raumer J.F., Ménot R.-P., Abrecht J., Biino G., 1993. The Pre-alpine evolution of the External massifs. In: von Raumer, J.F., Neubauer, F. (Eds.), Pre-Mesozoic Geology in the Alps. Springer-Verlag, Berlin Heidelberg, pp. 221–240.

Wood B.J., Blundy J.D., 1997. A predictive model for rare earth element partitioning between clinopyroxene and anhydrous silicate melt. Contrib. Mineral. Petrol. 129, 166–181.